Reference-Frame Selection on Impedance Modeling of VSCs With Fundamental Frequency Dynamics

Yang Wu, *Member, IEEE*, Heng Wu, *Senior Member, IEEE*, Fangzhou Zhao, *Member, IEEE*, Zichao Zhou, and Xiongfei Wang, *Fellow, IEEE*

***Abstract*—The fundamental frequency of ac power-electronic-based power systems may deviate from its nominal value, and it is highly affected by converter control dynamics. To capture the dynamics of fundamental frequency, two impedance modeling methods for voltage-source converters (VSCs) are reported, with respect to the selection of system reference frame. The first method is to model VSCs in a reference frame with the nominal frequency, while the second method models VSCs in a reference frame with varying fundamental frequency, and hence, the fundamental frequency is represented as an additional terminal variable in the impedance model. This article mathematically proves that the two impedance models are essentially equivalent, provided that the frequency dynamics is accounted in the modeling of control delay and power stage of VSCs in the second method. This equivalence is demonstrated for both grid-following (GFL) and grid-forming (GFM) VSCs. Stability predictions based on two methods are further compared based on an interconnected GFM and GFL VSC system. The results are also found to be identical. Finally, experiments validate the correctness of the theoretical analysis.**

***Index Terms*—Fundamental frequency dynamics, small-signal model, terminal characteristics, voltage-source converter (VSC).**

I. Introduction

TO ACCOMMODATE the large-scale integration of renewable energy resources, the legacy power grids that are based on synchronous generators (SGs) will gradually be replaced by highly renewable, power-electronic-based power systems [1], [2]. Differing from SGs with well-established physical models, dynamics of power converters are highly dependent on their control systems [3], [4], [5]. Consequently, the dynamic interactions of converters are significantly different from those of SGs, and they are tightly coupled with the electromagnetic dynamics of power networks, often manifesting undesired oscillations across multiple timescales.

In recent years, the impedance-based modeling and analysis method emerges as an attractive way to address the adverse control interactions of converters [6], [7], [8], [9]. Two commonly used impedance models are established in the rotating dq-frame and the stationary $\alpha\beta$-frame, respectively, [10], [11], [12]. Between these, the dq-frame impedance model has gained popularity due to its modeling convenience, as the control of grid-connected voltage-source converters (VSCs) is typically performed in the dq-frame [13]. Conventionally, this approach involves building two dq-frames aligned with the measured and actual grid phases, as shown in Fig. 1(a), which are commonly referred to as the controller frame and the system frame [14]. The dynamics of VSC synchronization controllers, e.g., phase-locked loop (PLL), is accounted by the transformation between these frames [10], and the impedance model of VSC is formulated in the system frame as a 2×2 matrix, whose inputs and outputs only contain voltage and current signals [15]. Yet, the impedance modeling of VSC is usually based on the assumption that the fundamental frequency of the reference system frame

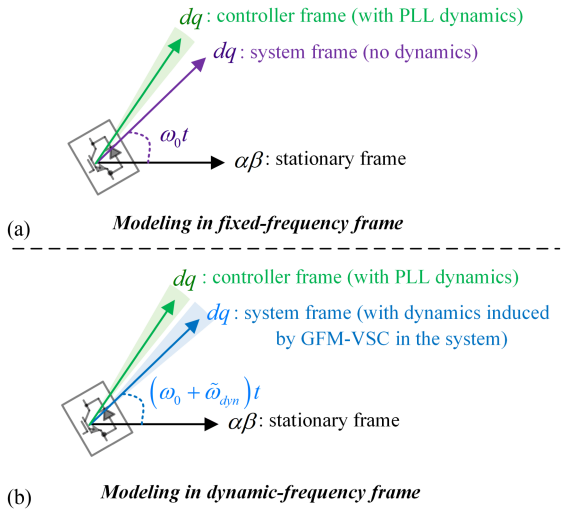

Fig. 1. Comparison of converter impedance modeling in (a) fixed-frequency and (b) dynamic-frequency frame. A GFL VSC is taken as an example. ω_0 denotes a constant angular rotating frequency of the system frame, normally corresponding to system operating frequency. $\tilde{\omega}_{\text{dyn}}$ represents the frequency dynamics of the system frame.

Received 27 November 2024; revised 19 January 2025; accepted 5 March 2025. Date of publication 10 March 2025; date of current version 14 April 2025. This work was supported by the European Union's Horizon 2020 Research and Innovation Program under the Marie Skłodowska-Curie Grant Agreement under Grant 101107634 (PhyDAWN). Recommended for publication by Associate Editor M. Saeedifard. *(Corresponding author: Xiongfei Wang.)*

Yang Wu, Heng Wu, and Fangzhou Zhao are with the AAU Energy, Aalborg University, 9220 Aalborg, Denmark (e-mail: yawu@energy.aau.dk; hew@energy.aau.dk; fzha@energy.aau.dk).

Zichao Zhou is with the Division of Electric Power and Energy Systems, KTH Royal Institute of Technology, 10044 Stockholm, Sweden (e-mail: zichaoz@kth.se).

Xiongfei Wang is with the Division of Electric Power and Energy Systems, KTH Royal Institute of Technology, 10044 Stockholm, Sweden, and also with the AAU Energy, Aalborg University, 9220 Aalborg, Denmark (e-mail: xiongfei@kth.se).

Color versions of one or more figures in this article are available at https://doi.org/10.1109/TPEL.2025.3549635.

Digital Object Identifier 10.1109/TPEL.2025.3549635

is fixed [16], [17], [18], [19], [20], [21], which is primarily applied to single-converter-infinite-bus system. This assumption may not hold for power-electronic-based power systems. The system frequency can be fully regulated by grid-forming (GFM) VSCs [22], [23], whose dynamics has a similar timescale with system harmonics. In addition, the physical interpretation of the impedances in the d and q axes is not sufficiently clear.

To address these challenges, it has recently been proposed to incorporate the fundamental frequency dynamics as an additional terminal variable in the impedance model of VSC [24], [25], [26], [27], and then the whole system is modeled in a reference system frame that rotates with a dynamic fundamental frequency (referred to as *dynamic-frequency frame* in the following text of this article). An illustration of this new modeling approach is presented in Fig. 1(b). Unlike the conventional approach, the derived impedance model is a 2×3 matrix for a selected reference VSC (typically a GFM-VSC) [24] and a 3×2 matrix for the other VSCs [26], as the inputs and outputs now contain fundamental frequency signal. This method performs well in predicting the stability of paralleled droop-controlled GFM-VSCs and of system comprising multiple GFM-VSCs and grid-following (GFL) VSCs [28], as the dynamic-frequency system frame aligned to a reference GFM-VSC can be directly used for the impedance modeling of other converters within the system. This method also offers greater physical insight into the interactions between VSC synchronization controllers [29], as the additional terminal variable is directly linked to the variations of system fundamental frequency.

Nevertheless, some research has pointed out that the dynamics of fundamental frequency may have already been embedded in the 2×2 impedance matrix in the conventional approaches [30] because terminal voltage and current signals inherently contain the information of fundamental frequency dynamics. Thus, the conventional impedance modeling approach is still effective: the impedance model of VSC can still be established in a reference system frame with the fixed frequency [31], [32] (referred to as *fixed-frequency frame* in the following text of this article). However, the mathematical relationship between these two reference-frame impedance models remains unclear.

This article attempts to fill the void. It is found that the two reference-frame (i.e., dynamic-frequency and fixed-frequency frames) impedance models of VSCs are mathematically equivalent, provided that the frequency dynamics is accounted into the modeling of control delay and power stage of VSC in the dynamic-frequency frame. An interconnected GFM-VSC and GFL-VSC system is taken as a case study to examine the correctness of theoretical findings. The main contributions of this article are as follows.

1) A step-by-step derivation on the equivalence of VSC impedance models in different reference frames is formulated, where the mathematical proof of modeling equivalence is provided at the VSC component level, including PLL, droop control, power stage, and control delay.
2) The model equivalence for GFM-VSC and GFL-VSC in the studied interconnected system is proved by means of the block diagram algebra, which is built on the modeling equivalence of VSC components.

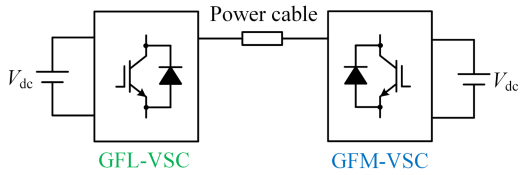

Fig. 2. Schematic diagram of the studied system.

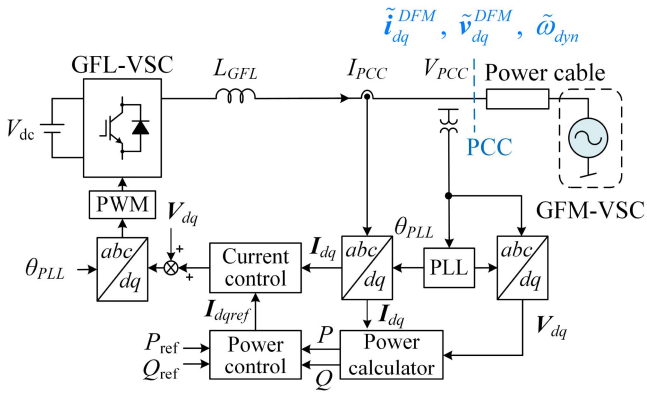

Fig. 3. One-line diagram of the GFL-VSC.

3) Stability prediction of the interconnected GFM-VSC and GFL-VSC system is proved to be equivalent with respect to the selection of system reference frame.

The rest of this article is organized as follows. The configuration of the studied system is presented in Section II. The modeling equivalence for VSC components associated with the system frame is demonstrated in Section III, followed by the demonstration of modeling equivalence for the studied system in Section IV. Simulation and experimental results are presented in Sections V and VI for the validation. Finally, Section VII concludes this article.

II. System Description

To generalize the findings in this article, an interconnected GFM-VSC and GFL-VSC system is studied, as shown in Fig. 2. Such structure can be found in high-voltage direct current integrated offshore wind farm and battery energy storage systems, which serves as an effective representative for power-electronic-based power systems [22]. An industry case of the studied system structure has also been presented in [33], where an offshore wind farm controlled in GFL mode is connected to an onshore modular multilevel converter station controlled in GFM mode.

The one-line diagram of the GFL-VSC is shown in Fig. 3. The dc-link voltage V_{dc} is assumed as constant. The converter is connected to the point of common coupling (PCC) through a filter inductor L_{GFL} [equivalent series resistance (ESR) = R_{GFL}]. The voltage V_{PCC} and current I_{PCC} at the PCC point are measured for the control. The reference current direction is defined as flowing out from the GFL-VSC into the GFM-VSC. A synchronous reference-frame phase-locked loop (SRF-PLL) is used, with θ_{PLL} denoting the phase angle. The converter is regulated as a constant power source by current controller and power controller in proportional–integral control (PI) form.

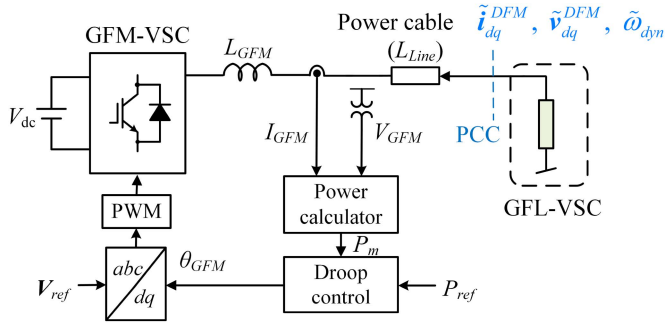

Fig. 4. One-line diagram of the studied GFM-VSC.

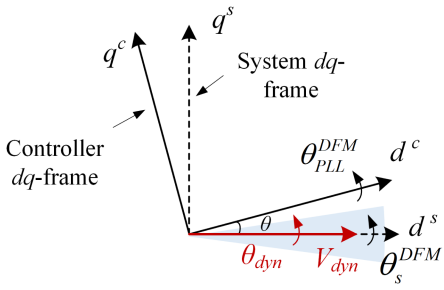

Fig. 5. Controller and system dq-frame with dynamic frequency, where $V_{\rm dyn}$ and $\theta_{\rm dyn}$ represent the voltage and phase angle of the grid formed by GFM-VSC.

Voltage feedforward control is also applied by adding the dq-axis voltage to the output of the current controller. The parameters of the controller and power stage are provided in Appendix A.

The GFM-VSC is connected to the PCC point through filter inductor $L_{\rm GFM}$ (ESR $= R_{\rm GFM}$) and line inductor $L_{\rm Line}$ (ESR $= R_{\rm Line}$), as shown in Fig. 4. A simplified GFM-VSC control structure is used in this article. The voltage $V_{\rm GFM}$ and current $I_{\rm GFM}$ are measured for the calculation of active power P_m. Droop control is used, which generates system fundamental frequency dynamics through output phase angle $\theta_{\rm GFM}$. The parameters of the GFM-VSC are also included in Appendix A.

III. Modeling Equivalence of VSC Components Between Different Reference Frames

A. Reference System Frame Selection for VSC Modeling

Fundamental frequency of power-electronic-based power system is regulated by GFM-VSCs, which may contain different kinds of dynamics. To capture the fundamental frequency dynamics, system frequency can be treated as a separate terminal variable of the impedance model and the entire system can be modeled referred to the system frame with this dynamic frequency [24]. This dynamic-frequency-frame model (abbreviated as *DFM* in the following text of this article) is very different from a widely adopted fixed-frequency-frame model without frequency as terminal variable (abbreviated as *FFM* in the following text of this article). A demonstration of the reference system frame selection can be found in Fig. 1.

It is shown that FFM is established in reference to a rotating system frame with fixed angular frequency ω_0 (normally the system operating frequency). By contrast, DFM is established in reference to a rotating system frame with dynamic fundamental frequency $\omega_0 + \tilde{\omega}_{\rm dyn}$. $\tilde{\omega}_{\rm dyn}$ represents the system frequency perturbation in angular format, which is generated by the GFM-VSC. It should be noted that the discussion scope of this article is still in small-signal modeling and analysis. Hence, the dynamics of fundamental frequency is regarded as small-signal perturbation.

Although DFM and FFM have been studied in the existing research, the relationship between them has not yet been fully clarified. The equivalence of these two models needs to be studied from two perspectives: First, since they are established in different system frames, it is necessary to analyze the component involved in the transformation between the system and controller frames (e.g., PLL and droop control), as well as those modeled directly in the system frame (e.g., power stage and control delay), to identify the conditions under which the two approaches are equivalent. Second, given the additional fundamental frequency terminal in the DFM, the feasibility of embedding frequency dynamics into the terminal voltage/current signals and transforming DFM into FFM must also be explored. In FFM, the embedment of frequency dynamics into terminal voltage/current signals is realized by transforming the perturbations of electrical signals $\tilde{\mathbf{x}}_{dq}$ ($\mathbf{x}$ can denote the voltage $\mathbf{v}$, current $\mathbf{i}$, and duty ratio $\mathbf{d}$) between dynamic-frequency frame and fixed-frequency frame using the first-order Taylor expansion [30], as follows:

$$\tilde{\mathbf{x}}_{dq} = \tilde{\mathbf{x}}_{dq}^{\rm DFM} e^{j\tilde{\theta}_{\rm dyn}} \approx \tilde{\mathbf{x}}_{dq}^{\rm DFM} + j\mathbf{X}_{dq0}\tilde{\theta}_{\rm dyn}. \tag{1}$$

$\tilde{\theta}_{\rm dyn}$ represents the phase angle perturbation, which is the integral of fundamental frequency dynamics $\tilde{\omega}_{\rm dyn}$. $\mathbf{X}_{dq0}$ represents the steady-state value. In the following text of this article, a step-by-step verification will be conducted, starting from the modeling equivalence between converter component in DFM and that using (1) in FFM.

In this article, bold letters are used for complex space vectors, and italic letters are used for real space vectors, e.g., $\mathbf{v}_{dq} = v_d + jv_q \leftrightarrow v_{dq} = [v_d, v_q]^T$. Subscript dq represents a rotating system frame, and subscript $\alpha\beta$ represents the stationary system frame. Superscript c denotes the controller frame. Subscript 0 denotes the steady-state value. Meanwhile, superscript DFM denotes the modeling in dynamic-frequency frame, and the transfer function matrices or space vectors without superscript DFM are expressed in the fixed-frequency frame as conventional. The small-signal representations of the variables are denoted with symbol "$\sim$".

B. Equivalence of PLL Modeling in Different System Frames

1) PLL Modeling in DFM: The PLL model in dynamic-frequency frame is first developed. The controller dq-frame and system dq-frame in DFM are shown in Fig. 5. In dynamic-frequency frame, phase angle of the system frame can be expressed as $\theta_s^{\rm DFM} = \theta_0 + \tilde{\theta}_{\rm dyn}$, where θ_0 represents the steady-state phase angle.

When modeled in DFM, all the signals are expressed in reference to this dynamic-frequency frame. Hence, recall the control diagram of an SRF-PLL, the equation of PLL can be derived as follows:

$$\tilde{\theta}_{\rm PLL}^{\rm DFM} = \frac{G_{\rm PLL}}{s}\tilde{v}_{qc}^{\rm DFM} \tag{2}$$

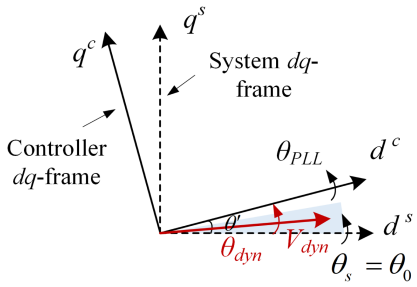

Fig. 6. Controller and system dq-frame with fixed frequency. Now, the reference system frame is not aligned to the grid phase angle with dynamics.

$$\mathbf{v}_{dqc}^{\mathrm{DFM}} = e^{-j\tilde{\theta}}\mathbf{v}_{dq}^{\mathrm{DFM}} \tag{3}$$

where $\theta_{\mathrm{PLL}}^{\mathrm{DFM}}$ denotes the phase angle of the PLL. G_{PLL} represents the transfer function of the PLL. θ represents the angle difference between the controller frame and the system frame, which satisfies

$$\tilde{\theta} = \tilde{\theta}_{\mathrm{PLL}}^{\mathrm{DFM}} - \tilde{\theta}_{s}^{\mathrm{DFM}} = \tilde{\theta}_{\mathrm{PLL}}^{\mathrm{DFM}} - \tilde{\theta}_{\mathrm{dyn}}. \tag{4}$$

The first-order approximation of (3) is then given by

$$\mathbf{v}_{dqc}^{\mathrm{DFM}} = \left(V_{d0} + \tilde{\mathbf{v}}_{dq}^{\mathrm{DFM}}\right) e^{-j\tilde{\theta}} \approx \left(V_{d0} + \tilde{\mathbf{v}}_{dq}^{\mathrm{DFM}}\right)\left(1 - j\tilde{\theta}\right) \tag{5}$$

which leads to

$$\tilde{v}_{qc}^{\mathrm{DFM}} \approx \tilde{v}_{q}^{\mathrm{DFM}} - V_{d0}\tilde{\theta} \tag{6}$$

assuming that the steady-state PCC voltage is aligned to the d-axis as V_{d0}.

Substituting (4) and (6) into (2), $\tilde{\theta}_{\mathrm{PLL}}^{\mathrm{DFM}}$ can be derived as follows:

$$\tilde{\theta}_{\mathrm{PLL}}^{\mathrm{DFM}} = \frac{G_{\mathrm{PLL}}}{s + G_{\mathrm{PLL}}V_{d0}}\tilde{v}_{q}^{\mathrm{DFM}} + \frac{G_{\mathrm{PLL}}V_{d0}}{s + G_{\mathrm{PLL}}V_{d0}}\tilde{\theta}_{\mathrm{dyn}}. \tag{7}$$

Using (4), the angle difference between the system frame and the controller frame satisfies

$$\tilde{\theta} = \frac{G_{\mathrm{PLL}}}{s + G_{\mathrm{PLL}}V_{d0}}\tilde{v}_{q}^{\mathrm{DFM}} - \frac{s}{s + G_{\mathrm{PLL}}V_{d0}}\tilde{\theta}_{\mathrm{dyn}}. \tag{8}$$

Compared with the conventional PLL models that are only affected by the q-axis voltage perturbations [14], it is shown that when the PLL is modeled in the dynamic-frequency frame, an additional term (highlighted in red) appears, which accounts for fundamental frequency dynamics. This indicates that the PLL model incorporates the frequency dynamics of the system frame.

2) PLL Modeling in FFM: By contrast, when the PLL is modeled in fixed-frequency frame with $\theta_s = \theta_0$, as shown in Fig. 6, the angle difference between the controller frame and the system frame θ' satisfies

$$\tilde{\theta}' = \tilde{\theta}_{\mathrm{PLL}}. \tag{9}$$

This is because now the system frame contains no dynamics. As in the conventional modeling approaches [14], [27], the control diagram of PLL then gives

$$\tilde{\theta}_{\mathrm{PLL}} = \frac{G_{\mathrm{PLL}}}{s}\tilde{v}_{qc} \tag{10}$$

$$\mathbf{v}_{dqc} = e^{-j\tilde{\theta}'}\mathbf{v}_{dq}. \tag{11}$$

The first-order approximation of (11) is then given by

$$\tilde{v}_{qc} \approx \tilde{v}_{q} - V_{d0}\tilde{\theta}'. \tag{12}$$

Therefore, the following equation can be derived:

$$\tilde{\theta}' = \tilde{\theta}_{\mathrm{PLL}} = \frac{G_{\mathrm{PLL}}}{s + G_{\mathrm{PLL}}V_{d0}}\tilde{v}_{q}. \tag{13}$$

To compare the PLL models in different system frames, the obtained phase angle of the PLL in different frames is studied. According to (1), the relationship between the voltage perturbation in DFM and FFM is

$$\tilde{\mathbf{v}}_{dq} \approx \tilde{\mathbf{v}}_{dq}^{\mathrm{DFM}} + jV_{dq0}\tilde{\theta}_{\mathrm{dyn}} \tag{14}$$

which leads to

$$\tilde{v}_{q} \approx \tilde{v}_{q}^{\mathrm{DFM}} + V_{d0}\tilde{\theta}_{\mathrm{dyn}}. \tag{15}$$

Therefore, by substituting (15) into (13), the PLL model in fixed-frequency frame can now be formulated as follows:

$$\tilde{\theta}' = \tilde{\theta}_{\mathrm{PLL}} = \frac{G_{\mathrm{PLL}}}{s + G_{\mathrm{PLL}}V_{d0}}\tilde{v}_{q}^{\mathrm{DFM}} + \frac{G_{\mathrm{PLL}}V_{d0}}{s + G_{\mathrm{PLL}}V_{d0}}\tilde{\theta}_{\mathrm{dyn}}. \tag{16}$$

Equation (16) shows that, although embedded into voltage in FFM, the fundamental frequency dynamics still takes effect on the output of the PLL (as marked out by the term highlighted in red). Comparing (7) and (16), it can be found that $\tilde{\theta}_{\mathrm{PLL}} = \tilde{\theta}_{\mathrm{PLL}}^{\mathrm{DFM}}$. Then, it can be derived that

$$\tilde{\theta}' = \tilde{\theta}_{\mathrm{PLL}} = \tilde{\theta}_{\mathrm{PLL}}^{\mathrm{DFM}} = \tilde{\theta} + \tilde{\theta}_{\mathrm{dyn}}. \tag{17}$$

It means that the controller frame and the PLL modeling in DFM and FFM are exactly identical.

It can then be proved that the electrical signals in the controller frame for DFM and FFM will also be identical. Taking voltage as an example, the following equations hold to unify the different models:

$$\text{DFM}\begin{cases}\tilde{v}_{d}^{c} = \tilde{v}_{d}^{\mathrm{DFM}} \\ \tilde{v}_{q}^{c} = \tilde{v}_{q}^{\mathrm{DFM}} - V_{d0}\tilde{\theta}\end{cases} \tag{18}$$

$$\text{FFM}\begin{cases}\tilde{v}_{d}^{c} = \tilde{v}_{d} = \tilde{v}_{d}^{\mathrm{DFM}} \\ \tilde{v}_{q}^{c} = \tilde{v}_{q} - V_{d0}\tilde{\theta}' = \left(\tilde{v}_{q}^{\mathrm{DFM}} + V_{d0}\tilde{\theta}_{\mathrm{dyn}}\right) - V_{d0}\tilde{\theta}' \\ \quad = \tilde{v}_{q}^{\mathrm{DFM}} - V_{d0}\tilde{\theta}.\end{cases} \tag{19}$$

C. Equivalence of Droop Controller Modeling in Different System Frames

For GFM-VSC, the difference between droop controller models in different reference frames lies in the calculation of active power P_m. Considering the linearization in power calculation, it can be developed for DFM that

$$\begin{aligned} P_{m}^{\mathrm{DFM}} &= v_{d}^{\mathrm{DFM}}i_{d}^{\mathrm{DFM}} + v_{q}^{\mathrm{DFM}}i_{q}^{\mathrm{DFM}} \\ &= \left(V_{d0} + \tilde{v}_{d}^{\mathrm{DFM}}\right)\left(I_{d0} + \tilde{i}_{d}^{\mathrm{DFM}}\right) \\ &\quad + \tilde{v}_{q}^{\mathrm{DFM}}\left(I_{q0} + \tilde{i}_{q}^{\mathrm{DFM}}\right) \\ &\approx V_{d0}I_{d0} + V_{d0}\tilde{i}_{d}^{\mathrm{DFM}} + I_{d0}\tilde{v}_{d}^{\mathrm{DFM}} + I_{q0}\tilde{v}_{q}^{\mathrm{DFM}}. \end{aligned} \tag{20}$$

Meanwhile, the calculation of active power for FFM can be developed as

$$P_m = v_d i_d + v_q i_q$$

$$
\begin{aligned}
&= (V_{d0} + \tilde{v}_d)\left(I_{d0} + \tilde{i}_d\right) + \tilde{v}_q\left(I_{q0} + \tilde{i}_q\right) \\
&= \left(V_{d0} + \tilde{v}_d^{\mathrm{DFM}}\right)\left(I_{d0} + \tilde{i}_d^{\mathrm{DFM}} - I_{q0}\tilde{\theta}_{\mathrm{dyn}}\right) \\
&\quad + \left(\tilde{v}_q^{\mathrm{DFM}} + V_{d0}\tilde{\theta}_{\mathrm{dyn}}\right)\left(I_{q0} + \tilde{i}_q^{\mathrm{DFM}} + I_{d0}\tilde{\theta}_{\mathrm{dyn}}\right) \\
&\approx V_{d0}I_{d0} + V_{d0}\tilde{i}_d^{\mathrm{DFM}} + I_{d0}\tilde{v}_d^{\mathrm{DFM}} + I_{q0}\tilde{v}_q^{\mathrm{DFM}}. \qquad (21)
\end{aligned}
$$

It is shown that $P_m^{\mathrm{DFM}} = P_m$. As the active power calculated in different frames is identical, the phase angle θ_{Droop} regulated by the droop controller G_{Droop} will also be the same. Similar to the analysis for PLL modeling in Section III-B, the controller frame and the droop control modeling of GFM-VSC will not be influenced by the reference-frame selection as well.

D. Equivalence of Power Stage Modeling in Different System Frames

The modeling of converter power stage in different frames is then studied. The power stage typically consists of passive components, such as filter inductor, capacitor, and resistive load. Take filter inductor as an example. When the inductor voltage and current are modeled in dynamic-frequency frame (DFM) [34], their relationship can be expressed as follows:

$$\tilde{\mathbf{v}}_{dq}^{\mathrm{DFM}} \approx (s + j\omega_0)\, L\tilde{\mathbf{i}}_{dq}^{\mathrm{DFM}} + jLI_{dq0}\tilde{\omega}_{\mathrm{dyn}}. \qquad (22)$$

By contrast, in fixed-frequency frame (FFM), the inductor will be simply modeled as

$$\tilde{\mathbf{v}}_{dq} = (s + j\omega_0)\, L\tilde{\mathbf{i}}_{dq}. \qquad (23)$$

To unify the expressions in (22) and (23), (1) is first substituted into (23) regarding the filter current

$$
\begin{aligned}
\tilde{\mathbf{v}}_{dq} &= (s + j\omega_0)\, L\left(\tilde{\mathbf{i}}_{dq}^{\mathrm{DFM}} + jI_{dq0}\tilde{\theta}_{\mathrm{dyn}}\right) \\
&= (s + j\omega_0)\, L\tilde{\mathbf{i}}_{dq}^{\mathrm{DFM}} + jsLI_{dq0}\tilde{\theta}_{\mathrm{dyn}} - \omega_0 LI_{dq0}\tilde{\theta}_{\mathrm{dyn}}. \qquad (24)
\end{aligned}
$$

Recalling that $s\tilde{\theta}_{\mathrm{dyn}} = \tilde{\omega}_{\mathrm{dyn}}$ and $V_{dq0} = j\omega_0 LI_{dq0}$, it can be obtained that

$$\tilde{\mathbf{v}}_{dq} - jV_{dq0}\tilde{\theta}_{\mathrm{dyn}} = (s + j\omega_0)\, L\tilde{\mathbf{i}}_{dq}^{\mathrm{DFM}} + jLI_{dq0}\tilde{\omega}_{\mathrm{dyn}}. \qquad (25)$$

It can be found that (25) is equivalent to (22) when applying $\tilde{\mathbf{v}}_{dq} = \tilde{\mathbf{v}}_{dq}^{\mathrm{DFM}} + jV_{dq0}\tilde{\theta}_{\mathrm{dyn}}$. Therefore, the modeling of inductor is of identical accuracy for DFM and FFM, and this conclusion also holds for the modeling of capacitor. As the resistive elements will not be influenced by frequency, their modeling will always be identical in different frames.

E. Modeling of Control Delay in Dynamic-Frequency Frame

Especially, the modeling of control delay, as shown in Fig. 7, in dynamic-frequency frame is studied in this article, which is often overlooked in the existing research. T_d represents the delay time, whose typical value is 1.5 times of the sampling period T_s. The subscript del represents the variables or vectors after delay.

To obtain a more accurate small-signal model of control delay under fundamental frequency dynamics, Phase A is taken for analysis as

$$d_A^{\mathrm{del}} = e^{-sT_d} d_A. \qquad (26)$$

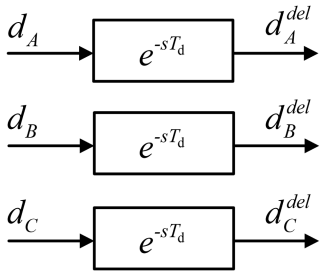

Fig. 7. Delay in the digital control.

As the switching frequency is normally much larger than the frequency range of interest, (26) can be approximated as

$$d_A^{\mathrm{del}} \approx (1 - sT_d)\, d_A \qquad (27)$$

where Taylor expansion is used to simplify the analysis. Although (27) is based on a first-order expansion of (26), it mainly aims to transform the frequency dynamics from system *abc*-frame to *dq*-frame more conveniently. This means that the transfer function between the duty ratio after delay ($\mathbf{d}_{dq-\mathrm{DFM}}^{\mathrm{del}}$) and the duty ratio before it ($\mathbf{d}_{dq-\mathrm{DFM}}$) can still be modeled using Pade approximation for accuracy, only with an additional term related to $\tilde{\omega}_{\mathrm{dyn}}$.

It is worth to be noted that the form of (27) is very similar to the expression of an inductor in series of a resistor. Under such assumption, $(1-sT_d)$ can be denoted as $R_{\mathrm{DEL}} + sL_{\mathrm{DEL}}$. R_{DEL} represents the equivalent resistance, which is equal to 1, and L_{DEL} represents the equivalent inductance, which is equal to $-T_d$. Adopting a similar expression as an inductor in *dq*-frame, the following equation can be obtained:

$$\mathbf{d}_{dq-\mathrm{DFM}}^{\mathrm{del}} \approx (1 - sT_d - j\,(\omega_0 + \tilde{\omega}_{\mathrm{dyn}})\, T_d)\, \mathbf{d}_{dq-\mathrm{DFM}}. \qquad (28)$$

A formal derivation for (28) can be found in Appendix B. Based on (28), the first-order approximation can be made, and the model of delay can be derived as

$$\mathbf{d}_{dq-\mathrm{DFM}}^{\mathrm{del}} = \mathbf{G}_{\mathrm{DEL}}\mathbf{d}_{dq-\mathrm{DFM}} - j\tilde{\omega}_{\mathrm{dyn}}T_d D_{dq0} \qquad (29)$$

where $\mathbf{G}_{\mathrm{DEL}}$ represents the transfer function matrix between the input and output of the delay. Equation (29) shows that the fundamental frequency dynamics leads to an additional term (the term highlighted in red) for the small-signal modeling of control delay in dynamic-frequency frame, whose coefficient is determined by both the delay time and the steady-state duty ratio. Furthermore, this deviation is irrelevant to the inspected frequency and will influence the delay modeling accuracy at both the low-frequency and medium-frequency range, which is always misjudged in the existing research. Similar to the analysis in Section III-D, the modeling accuracy of delay will not be influenced by different reference-frame selections.

In conclusion, the above analysis proves that the modeling accuracy for the converter components associated with the system frame is effectively equivalent for both DFM and FFM, provided that an additional frequency-related term is incorporated into the modeling of power stage and control delay. A summary of the component models in different system frames is presented in Table I. Since the controller frames are identically selected

TABLE I
COMPONENT MODELS ASSOCIATED WITH DIFFERENT SYSTEM FRAMES

	Model in DFM	Model in FFM
PLL	$\tilde{\theta}_{PLL}^{DFM}=\frac{G_{PLL}}{s+G_{PLL}V_{d0}}\tilde{v}_q^{DFM}+\frac{G_{PLL}V_{d0}}{s+G_{PLL}V_{d0}}\tilde{\theta}_{dyn}$	$\tilde{\theta}_{PLL}=\frac{G_{PLL}}{s+G_{PLL}V_{d0}}\tilde{v}_q$
Droop controller	$\tilde{\theta}_{Droop}^{DFM}=G_{Droop}\tilde{P}_m^{DFM}$	$\tilde{\theta}_{Droop}=G_{Droop}\tilde{P}_m$
Power stage (e.g., inductor)	$\tilde{\mathbf{v}}_{dq}^{DFM}\approx(s+\mathrm{j}\omega_0)L\tilde{\mathbf{i}}_{dq}^{DFM}+\mathrm{j}LI_{dq0}\tilde{\omega}_{dyn}$	$\tilde{\mathbf{v}}_{dq}=(s+\mathrm{j}\omega_0)L\tilde{\mathbf{i}}_{dq}$
Control delay	$\mathbf{d}_{dq-DFM}^{del}=\mathbf{G}_{DEL}\mathbf{d}_{dq-DFM}-\mathrm{j}\tilde{\omega}_{dyn}T_dD_{dq0}$	$\mathbf{d}_{dq}^{del}=\mathbf{G}_{DEL}\mathbf{d}_{dq}$

for both DFM and FFM, other controller components will have identical models in both frames and are, therefore, not further discussed.

IV. MODELING EQUIVALENCE FOR STUDIED SYSTEM

In this section, modeling equivalence for the studied interconnected system will further be proved. The primary focus is on addressing the integration of the additional fundamental frequency terminal in the DFM.

A. Model Transformation Between DFM and FFM

The key differences between models for the interconnected system in DFM and FFM are summarized in Table II. In FFM, the GFM-VSC is modeled as an impedance matrix $\mathbf{Z}_{\mathrm{GFM}}$ based on Thévenin equivalent circuit, and the GFL-VSC is modeled as an admittance matrix $\mathbf{Y}_{\mathrm{GFL}}$ based on Norton equivalent circuit. A minus sign exists as the reference current direction is defined as flowing out from the GFL-VSC and into the GFM-VSC. In DFM, apart from the impedance matrix $\mathbf{Z}_{\mathrm{GFM}}^{\mathrm{DFM}}$ for the GFM-VSC and the admittance matrix $\mathbf{Y}_{\mathrm{GFL}}^{\mathrm{DFM}}$ for the GFL-VSC (now expressed in the dynamic-frequency frame), two other transfer function matrices are introduced to describe the influence of frequency dynamics. $\mathbf{T}_{\omega\mathrm{GFM}}$ represents the response of fundamental frequency of GFM-VSC due to the input current perturbations, indicating that GFM-VSC generates the fundamental frequency dynamics in the system. $\mathbf{T}_{\omega\mathrm{GFL}}$ represents the response of output current of GFL-VSC from this fundamental frequency perturbation. Hence, the model of GFM-VSC in DFM can be expressed as a 2×3 matrix, where the input signals are current, and the output signals are voltage and frequency. By contrast, the model of GFL-VSC in DFM can be expressed as a 3×2 matrix, with reversed input and output signals compared with the GFM-VSC model. $\tilde{v}_{\mathrm{eq}}$ and $\tilde{i}_{\mathrm{eq}}$ are the equivalent voltage source and current source to characterize the influence of $\mathbf{T}_{\omega\mathrm{GFM}}$ and $\mathbf{T}_{\omega\mathrm{GFL}}$, respectively.

To unify DFM and FFM for the studied system, it is assumed that treating fundamental frequency as terminal variable (in DFM) is equivalent to embedding the frequency dynamics into local voltage/current signals at the terminal (in FFM) [30]. Based on this assumption, the generated fundamental frequency dynamics at the terminal of the GFM-VSC is first incorporated into the terminal voltage. According to (1) and DFM of GFM-VSC, as shown in Table II

$$\begin{aligned}\tilde{\mathbf{v}}_{dq}&\approx\tilde{\mathbf{v}}_{dq}^{\mathrm{DFM}}+j\mathbf{V}_{dq0}\tilde{\theta}_{\mathrm{dyn}}\Rightarrow\\ \tilde{v}_{dq}&\approx\tilde{v}_{dq}^{\mathrm{DFM}}+[0\quad V_{d0}]^T\tilde{\theta}_{\mathrm{dyn}}\\&=\tilde{v}_{dq}^{\mathrm{DFM}}+[0\quad V_{d0}]^T\frac{\tilde{\omega}_{\mathrm{dyn}}}{s}\\&=\mathbf{Z}_{\mathrm{GFM}}^{\mathrm{DFM}}\tilde{i}_{dq}^{\mathrm{DFM}}+[0\quad V_{d0}]^T\frac{1}{s}\mathbf{T}_{\omega\mathrm{GFM}}\tilde{i}_{dq}^{\mathrm{DFM}}.\end{aligned}\tag{30}$$

Then, $\tilde{i}_{dq}^{\mathrm{DFM}}$ needs to be transformed into the fixed-frequency frame for the unification. This can be done based on (1) and FFM of GFL-VSC in Table II

$$\begin{aligned}\tilde{\mathbf{i}}_{dq}&\approx\tilde{\mathbf{i}}_{dq}^{\mathrm{DFM}}+j\mathbf{I}_{dq0}\tilde{\theta}_{\mathrm{dyn}}\Rightarrow\\ \tilde{i}_{dq}^{\mathrm{DFM}}&=\tilde{i}_{dq}+[I_{q0}\quad -I_{d0}]^T\tilde{\theta}_{\mathrm{dyn}}\\&=\tilde{i}_{dq}+[I_{q0}\quad -I_{d0}]^T\frac{\tilde{\omega}_{\mathrm{dyn}}}{s}\\&=-\mathbf{Y}_{\mathrm{GFL}}\tilde{v}_{dq}+[I_{q0}\quad -I_{d0}]^T\frac{1}{s}\mathbf{T}_{\omega\mathrm{GFM}}\tilde{i}_{dq}^{\mathrm{DFM}}.\end{aligned}\tag{31}$$

Based on (30) and (31), the embedment of fundamental frequency dynamics into terminal signals can be achieved in Fig. 8.

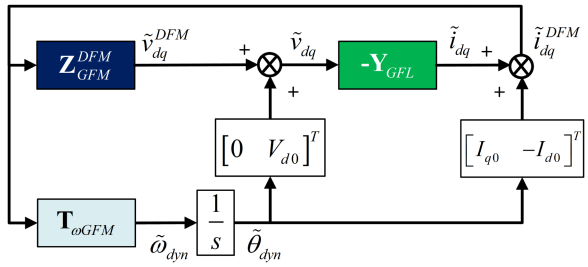

Fig. 8. Transformation block diagram for the unification of DFM and FFM.

Therefore, the equivalence of DFM and FFM for the studied interconnected system can be proved by their transformation to the block diagram in Fig. 8. By comparing the system models in Table II and Fig. 8, it can be found that the transformation between DFM and the block diagram in Fig. 8 depends on the solidness of (32), while the transformation between the block diagram in Fig. 8 and FFM depends on the solidness of (33)

$$\begin{aligned}\mathbf{T}_{\omega\mathrm{GFL}}&=\frac{1}{s}\left(-\mathbf{Y}_{\mathrm{GFL}}^{\mathrm{DFM}}\right)\begin{bmatrix}0\\V_{d0}\end{bmatrix}+\frac{1}{s}\begin{bmatrix}I_{q0}\\-I_{d0}\end{bmatrix}\\&=\frac{1}{s}\left(-\mathbf{Y}_{\mathrm{GFL}}\right)\begin{bmatrix}0\\V_{d0}\end{bmatrix}+\frac{1}{s}\begin{bmatrix}I_{q0}\\-I_{d0}\end{bmatrix}\end{aligned}\tag{32}$$

$$\begin{aligned}\mathbf{Z}_{\mathrm{GFM}}&=\left(\mathbf{Z}_{\mathrm{GFM}}^{\mathrm{DFM}}+\frac{1}{s}\begin{bmatrix}0\\V_{d0}\end{bmatrix}\mathbf{T}_{\omega\mathrm{GFM}}\right)\\&\quad\times\left(\mathbf{I}-\frac{1}{s}\begin{bmatrix}I_{q0}\\-I_{d0}\end{bmatrix}\mathbf{T}_{\omega\mathrm{GFM}}\right)^{-1}\end{aligned}\tag{33}$$

TABLE II
DIFFERENT MODELS FOR THE INTERCONNECTED SYSTEM IN DFM AND FFM

	Model in Dynamic-Frequency Frame (DFM)	Model in Fixed-Frequency Frame (FFM)
Equivalent Circuit	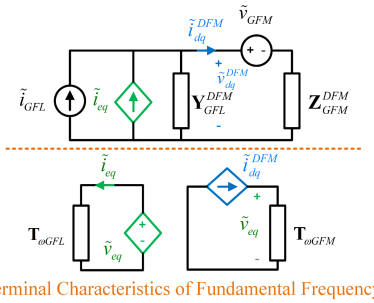	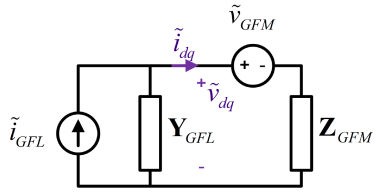
System Model	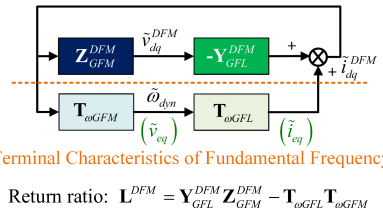 Return ratio: $\mathbf{L}^{DFM}=\mathbf{Y}_{GFL}^{DFM}\mathbf{Z}_{GFM}^{DFM}-\mathbf{T}_{\omega GFL}\mathbf{T}_{\omega GFM}$	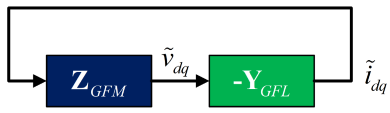 Return ratio: $\mathbf{L}=\mathbf{Y}_{GFL}\mathbf{Z}_{GFM}$

TABLE III
MAXIMUM ABSOLUTE ERROR BETWEEN MODELING AND SIMULATION RESULTS FOR $\mathbf{T}_{\omega\mathrm{GFL}}$

		Proposed model	Traditional model neglecting frequency dynamics on power stage	Traditional model neglecting frequency dynamics on control delay
d-axis	Magnitude (dB)	0.7929	7.5473	7.5265
	Phase (°)	8.5410	341.3195	341.4841
q-axis	Magnitude (dB)	0.6444	3.1762	7.4166
	Phase (°)	15.3800	39.3978	16.7818

where $\mathbf{I}$ represents the identity matrix. In (32), $\mathbf{Y}_{\mathrm{GFL}}^{\mathrm{DFM}}$ is equal to $\mathbf{Y}_{\mathrm{GFL}}$ because $\mathbf{Y}_{\mathrm{GFL}}^{\mathrm{DFM}}$ represents the current response of the GFL-VSC when $\tilde{\omega}_{\mathrm{dyn}}$ is set as zero, identically defined as $\mathbf{Y}_{\mathrm{GFL}}$. Therefore, $\mathbf{Y}_{\mathrm{GFL}}$ is used for both DFM and FFM in the following text of this article for simplicity.

To validate (32) and (33), DFM and FFM for GFL-VSC and GFM-VSC need to be developed and analyzed. The modeling equivalence of VSC components in Section III enables convenient converter model transformation between different frames by block diagram algebra, with GFL-VSC first taken as an example to prove the solidness of (32). The solidness of (33) for GFM-VSC can be analyzed in a similar manner and will be explained afterward. The stability of the entire system will be proved to be identical for DFM and FFM at the end of this section.

B. Model Equivalence Regarding GFL-VSC

To verify the relationship between $\mathbf{Y}_{\mathrm{GFL}}$ and $\mathbf{T}_{\omega\mathrm{GFL}}$ in (32), the accurate modeling of $\mathbf{T}_{\omega\mathrm{GFL}}$ needs to be developed first. As the modeling of $\mathbf{Y}_{\mathrm{GFL}}$ has already been detailed in many existing research [14], [35], it will not be repeated in this article.

Based on the modeling of PLL, filter, and control delay in Section III, the complete small-signal model for the studied GFL-VSC under fundamental frequency perturbations can be derived as Fig. 9. All the transfer function matrices related to the frequency dynamics have been marked in yellow, which are further summarized as follows:

$$\mathbf{G}_{fi-\mathrm{PLL}}=\begin{bmatrix} I_{q0}G_{f-\mathrm{PLL}} \\ -I_{d0}G_{f-\mathrm{PLL}}\end{bmatrix} \tag{34}$$

$$\mathbf{G}_{fv-\mathrm{PLL}}=\begin{bmatrix} 0 \\ -V_{d0}G_{f-\mathrm{PLL}}\end{bmatrix} \tag{35}$$

$$\mathbf{G}_{fd-\mathrm{PLL}}=\begin{bmatrix} -D_{q0}G_{f-\mathrm{PLL}} \\ D_{d0}G_{f-\mathrm{PLL}}\end{bmatrix} \tag{36}$$

$$\mathbf{G}_{f-\mathrm{del}}=\begin{bmatrix} T_dD_{q0} \\ -T_dD_{d0}\end{bmatrix} \tag{37}$$

$$\mathbf{L}_{\omega}=\frac{L_{\mathrm{GFL}}}{\left(sL_{\mathrm{GFL}}+R_{\mathrm{GFL}}\right)^2+{\omega_0}^2{L_{\mathrm{GFL}}}^2}\times\begin{bmatrix}\left(sL_{\mathrm{GFL}}+R_{\mathrm{GFL}}\right)I_{q0}-\omega_0L_{\mathrm{GFL}}I_{d0} \\ -\left(sL_{\mathrm{GFL}}+R_{\mathrm{GFL}}\right)I_{d0}-\omega_0L_{\mathrm{GFL}}I_{q0}\end{bmatrix}. \tag{38}$$

As the voltage and frequency perturbations are treated separately in the small-signal modeling, $\tilde{v}_{dq}^{\mathrm{DFM}}$ is set as zero when modeling $\mathbf{T}_{\omega\mathrm{GFL}}$. $G_{f-\mathrm{PLL}}$ represents the transfer function between the output of the PLL and the fundamental frequency perturbations. According to (8), $G_{f-\mathrm{PLL}}$ can be expressed as follows:

$$G_{f-\mathrm{PLL}}=-\frac{1}{s+G_{\mathrm{PI}}V_{d0}}. \tag{39}$$

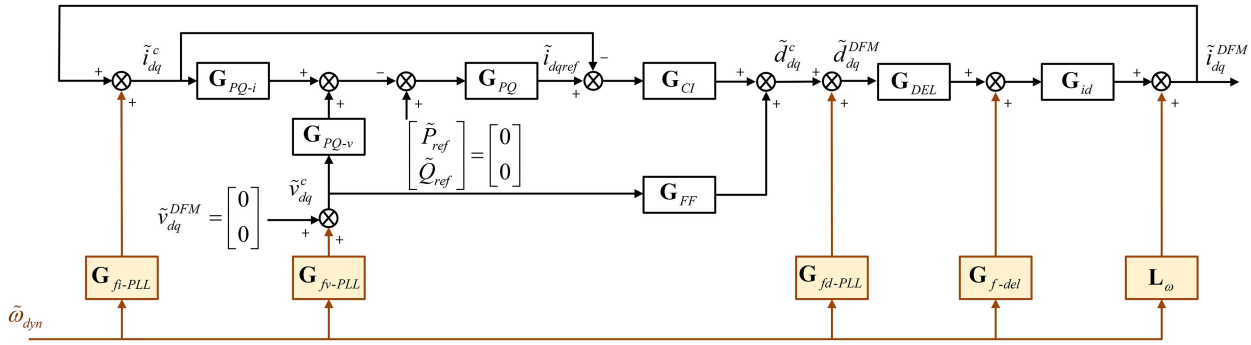

Fig. 9. Block diagram for the small-signal model of GFL-VSC under fundamental frequency perturbations.

The rest of the transfer function matrices are identical to the conventional impedance modeling of GFL-VSC: $\mathbf{G}_{PQ-i}$ and $\mathbf{G}_{PQ-v}$ denote the linearized transfer function matrices of power calculation. $\mathbf{G}_{PQ}$ and $\mathbf{G}_{CI}$ are the transfer function matrices of the power and current controller, respectively. $\mathbf{G}_{\mathrm{FF}}$ is an identity matrix representing the voltage feedforward control. $\mathbf{G}_{id}$ represents the transfer function matrix between the duty ratio and output current. $\mathbf{G}_{\mathrm{DEL}}$ represents the control delay. The detailed expressions of these matrices have been included in Appendix C. Therefore, the small-signal model of GFL-VSC under terminal fundamental frequency perturbations can be expressed as (40) shown at the bottom of this page:

Based on the block diagram of $\mathbf{T}_{\omega\mathrm{GFL}}$, the solidness of (32) can be studied. According to the impedance modeling of GFL-VSC [14], $\mathbf{Y}_{\mathrm{GFL}}$ can be derived and the block diagram of $\frac{1}{s}(-\mathbf{Y}_{\mathrm{GFL}})\begin{bmatrix}0\\V_{d0}\end{bmatrix}+\frac{1}{s}\begin{bmatrix}I_{q0}\\-I_{d0}\end{bmatrix}$ can be formulated as Fig. 10(a). It can be observed that the main difference between the block diagrams in Figs. 9 and 10(a) lies in the PLL, power stage, and control delay modeling.

The transfer function matrix $\mathbf{G}_{i-\mathrm{PLL}}$, which reflects the influence of PLL on controller current in $\mathbf{Y}_{\mathrm{GFL}}$, can be expressed as

$$\mathbf{G}_{i-\mathrm{PLL}}=\begin{bmatrix}0 & I_{q0}\frac{G_{\mathrm{PI}}}{s+V_{d0}G_{\mathrm{PI}}}\\ 0 & -I_{d0}\frac{G_{\mathrm{PI}}}{s+V_{d0}G_{\mathrm{PI}}}\end{bmatrix}. \tag{41}$$

Comparing (41) with (34), it can be derived that

$$\begin{aligned}\mathbf{G}_{fi-\mathrm{PLL}}&=\begin{bmatrix}-I_{q0}\frac{1}{s+V_{d0}G_{\mathrm{PI}}}\\ I_{d0}\frac{1}{s+V_{d0}G_{\mathrm{PI}}}\end{bmatrix}\\&=\frac{1}{s}\left(-\begin{bmatrix}I_{q0}\\-I_{d0}\end{bmatrix}+\mathbf{G}_{i-\mathrm{PLL}}\begin{bmatrix}0\\V_{d0}\end{bmatrix}\right).\end{aligned} \tag{42}$$

Similarly, the expression of $\mathbf{G}_{v-\mathrm{PLL}}$ is shown as

$$\mathbf{G}_{v-\mathrm{PLL}}=\begin{bmatrix}1 & 0\\ 0 & 1-V_{d0}\frac{G_{\mathrm{PI}}}{s+V_{d0}G_{\mathrm{PI}}}\end{bmatrix}. \tag{43}$$

The relationship between $\mathbf{G}_{v-\mathrm{PLL}}$ and $\mathbf{G}_{fv-\mathrm{PLL}}$ can be derived as

$$\mathbf{G}_{fv-\mathrm{PLL}}=\begin{bmatrix}0\\ V_{d0}\frac{1}{s+V_{d0}G_{\mathrm{PI}}}\end{bmatrix}=\frac{1}{s}\mathbf{G}_{v-\mathrm{PLL}}\begin{bmatrix}0\\V_{d0}\end{bmatrix}. \tag{44}$$

The expression of $\mathbf{G}_{d-\mathrm{PLL}}$ is shown in the following equation and the relationship between $\mathbf{G}_{d-\mathrm{PLL}}$ and $\mathbf{G}_{fd-\mathrm{PLL}}$ can also be derived:

$$\mathbf{G}_{d-\mathrm{PLL}}=\begin{bmatrix}0 & -D_{q0}\frac{G_{\mathrm{PI}}}{s+V_{d0}G_{\mathrm{PI}}}\\ 0 & D_{d0}\frac{G_{\mathrm{PI}}}{s+V_{d0}G_{\mathrm{PI}}}\end{bmatrix} \tag{45}$$

$$\begin{aligned}\mathbf{G}_{fd-\mathrm{PLL}}&=\begin{bmatrix}D_{q0}\frac{1}{s+V_{d0}G_{\mathrm{PI}}}\\ -D_{d0}\frac{1}{s+V_{d0}G_{\mathrm{PI}}}\end{bmatrix}\\&=\frac{1}{s}\left(-\begin{bmatrix}-D_{q0}\\D_{d0}\end{bmatrix}+\mathbf{G}_{d-\mathrm{PLL}}\begin{bmatrix}0\\V_{d0}\end{bmatrix}\right).\end{aligned} \tag{46}$$

In the above analysis, D_{d0} and D_{q0} represent the steady-state duty ratio before the delay. D_{d0}^{del} and D_{d0}^{del} represent the steady-state duty ratio after the delay.

Hence, to unify the expressions of $\mathbf{T}_{\omega\mathrm{GFL}}$ and $\mathbf{Y}_{\mathrm{GFL}}$, the equivalent block diagram of Fig. 10(a) can be replotted as Fig. 10(b). Furthermore, for the control delay, the following equation holds for the steady-state conditions:

$$\begin{aligned}&\mathbf{G}_{\mathrm{DEL}}\begin{bmatrix}-D_{q0}\\D_{d0}\end{bmatrix}-\begin{bmatrix}-D_{q0}^{\mathrm{del}}\\D_{d0}^{\mathrm{del}}\end{bmatrix}\\&\approx\begin{bmatrix}1-sT_d & 0\\ 0 & 1-sT_d\end{bmatrix}\begin{bmatrix}-D_{q0}\\D_{d0}\end{bmatrix}-\begin{bmatrix}-D_{q0}^{\mathrm{del}}\\D_{d0}^{\mathrm{del}}\end{bmatrix}\\&\approx-sT_d\begin{bmatrix}-D_{q0}\\D_{d0}\end{bmatrix}\approx s\mathbf{G}_{f-\mathrm{del}}.\end{aligned} \tag{47}$$

$$\begin{aligned}\mathbf{T}_{\omega\mathrm{GFL}}=&\left(\mathbf{I}+\mathbf{G}_{id}\mathbf{G}_{\mathrm{DEL}}\mathbf{G}_{CI}\left(\mathbf{I}+\mathbf{G}_{PQ}\mathbf{G}_{PQ-i}\right)\right)^{-1}\\&\times\left(\mathbf{L}_{\omega}+\mathbf{G}_{id}\left(\mathbf{G}_{f-\mathrm{del}}+\mathbf{G}_{\mathrm{DEL}}\left(\mathbf{G}_{fd-\mathrm{PLL}}+\mathbf{G}_{\mathrm{FF}}\mathbf{G}_{fv-\mathrm{PLL}}-\mathbf{G}_{CI}\left(\mathbf{G}_{fi-\mathrm{PLL}}-\mathbf{G}_{PQ}\right.\right.\right.\right.\right.\\&\times\left.\left.\left.\left.\left.\left(\mathbf{G}_{PQ-i}\mathbf{G}_{fi-\mathrm{PLL}}+\mathbf{G}_{PQ-v}\mathbf{G}_{fv-\mathrm{PLL}}\right)\right)\right)\right)\right).\end{aligned} \tag{40}$$

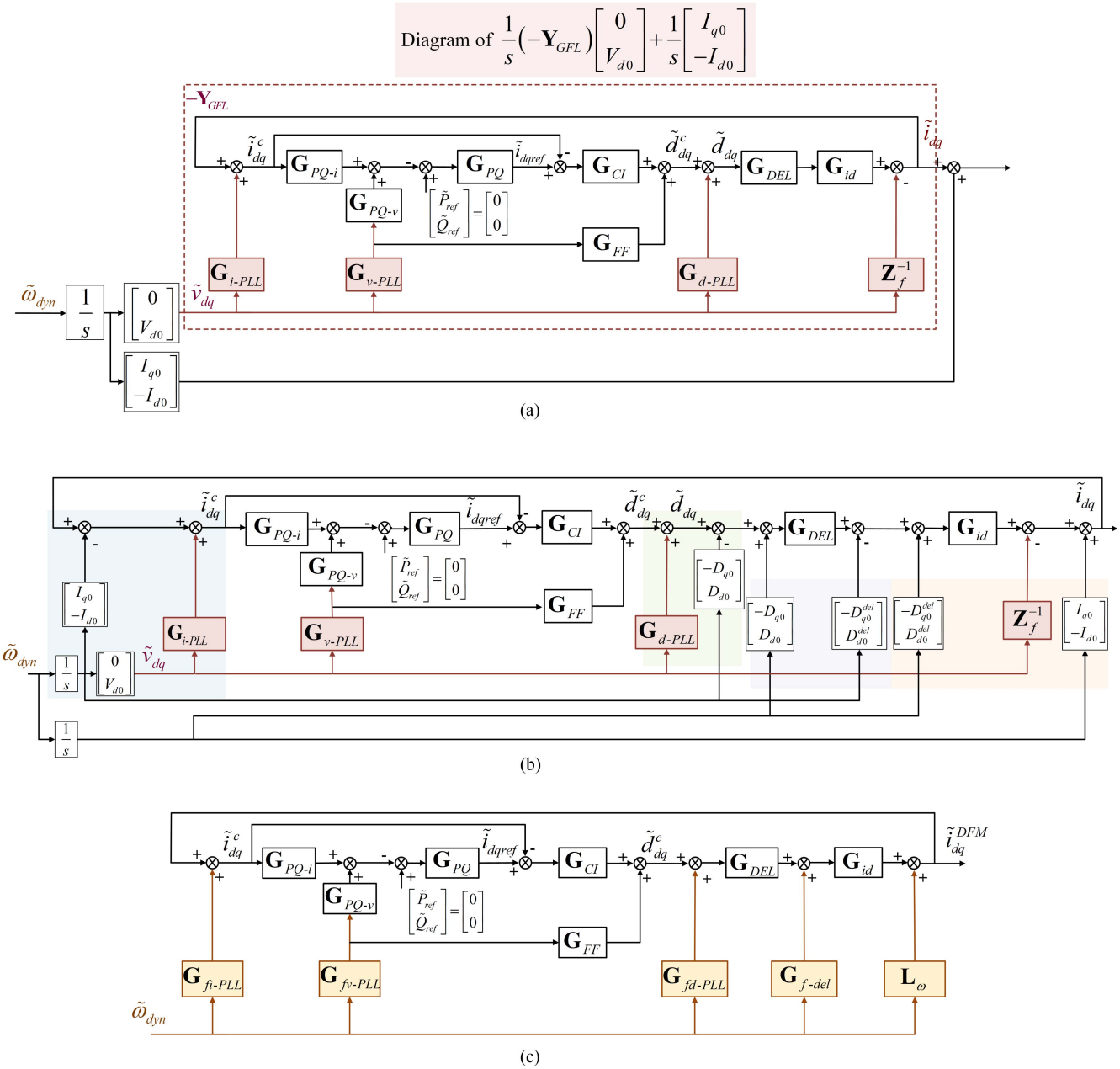

Fig. 10. Block diagram transformation for the unification of DFM and FFM models based on (32), (a)–(c) show different stages of the unification.

According to the circuit theory, for the filter inductor, we have

$$\mathbf{D}^{\text{del}}_{dq0} = \mathbf{V}_{dq0} + j\omega_0 L_{\text{GFL}}\mathbf{I}_{dq0}. \tag{48}$$

By multiplying j to (48), it can be derived that

$$\begin{aligned}
&\mathbf{G}_{id}\begin{bmatrix}-D^{\text{del}}_{q0}\\D^{\text{del}}_{d0}\end{bmatrix} - \mathbf{Z}_f^{-1}\begin{bmatrix}0\\V_{d0}\end{bmatrix} + \begin{bmatrix}I_{q0}\\-I_{d0}\end{bmatrix}\\
&= \mathbf{Z}_f^{-1}\left(\mathbf{Z}_f - \mathbf{Z}_{f0}\right)\begin{bmatrix}I_{q0}\\-I_{d0}\end{bmatrix}\\
&= sL_f\mathbf{Z}_f^{-1}\begin{bmatrix}I_{q0}\\-I_{d0}\end{bmatrix}\\
&= s\mathbf{L}_{\omega}
\end{aligned} \tag{49}$$

where $\mathbf{Z}_{f0}$ denotes $\begin{bmatrix}0 & -\omega_0 L_{\text{GFL}}\\ \omega_0 L_{\text{GFL}} & 0\end{bmatrix}$.

Therefore, by combining the different parts in Fig. 10(b) together, it is found that Fig. 10(b) is equivalent to Fig. 10(c), proving the solidness of (32): $\mathbf{T}_{\omega\text{GFL}}$ in DFM and $\frac{1}{s}(-\mathbf{Y}_{\text{GFL}})\begin{bmatrix}0\\V_{d0}\end{bmatrix}+\frac{1}{s}\begin{bmatrix}I_{q0}\\-I_{d0}\end{bmatrix}$ from FFM are identical. In conclusion, due to the modeling equivalence of components associated with the system frame, the overall converter model can be unified for both DFM and FFM. This unification occurs because the controller input remains identical, given the equivalence of PLL modeling in DFM and FFM, leading to the same controller output. Moreover, the output voltage of the converter has an identical effect on the output current due to the equivalent

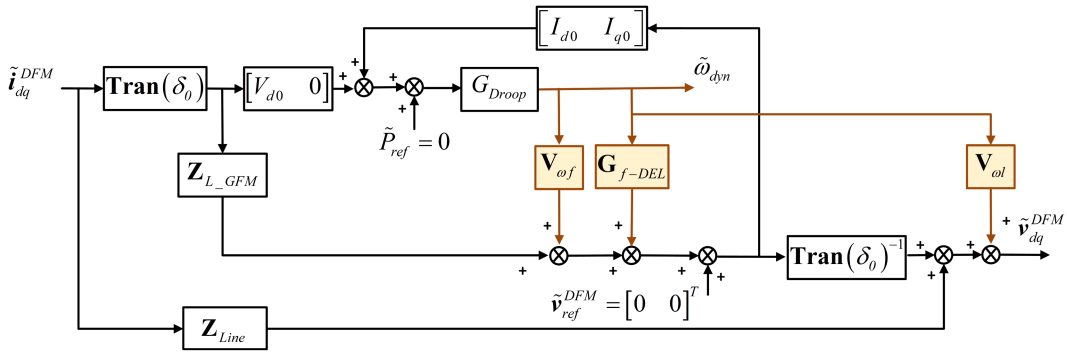

Fig. 11. Block diagram for the small-signal model of GFM-VSC in dynamic-frequency frame.

modeling of power stage and control delay. Ultimately, this results in an equivalent overall model for the GFL-VSC. In addition, it can be concluded that $\mathbf{T}_{\omega\mathrm{GFL}}$ does not need to be separately measured in practices, as it can be calculated based on the measured $\mathbf{Y}_{\mathrm{GFL}}$ and steady-state operating points.

C. Model Equivalence Regarding GFM-VSC

The model equivalence will also be demonstrated for the GFM-VSC by the validation of (33). Section III-C has proved that the controller frame and the droop controller modeling for a GFM-VSC will remain equivalent across different reference frames. Furthermore, the modeling of power stage and control delay will also be of equal accuracy as in the former analysis, leading to the solidness of (33).

To validate this assumption, the expression of $\mathbf{T}_{\omega\mathrm{GFM}}$ and $\mathbf{Z}_{\mathrm{GFM}}^{\mathrm{DFM}}$ for the GFM-VSC in dynamic-frequency frame needs to be developed, with the block diagram, as shown in Fig. 11. The effects of fundamental frequency dynamics on the modeling of filter inductor and control delay have been taken into account.

As shown in Fig. 11, $\mathbf{T}_{\omega\mathrm{GFM}}$ and $\mathbf{Z}_{\mathrm{GFM}}^{\mathrm{DFM}}$ can be summarized as follows:

$$\begin{aligned}\mathbf{T}_{\omega\mathrm{GFM}} = {} & (\mathbf{I} - G_{\mathrm{Droop}}(\mathbf{G}_{P-i}\mathbf{V}_{\omega f} \\ & + \mathbf{G}_{P-v}\mathbf{Z}_{L\_\mathrm{GFM}}\mathbf{G}_{f-\mathrm{DEL}}))^{-1} \\ & \times G_{\mathrm{Droop}}(\mathbf{G}_{P-i}\mathbf{Tran}(\delta_0) \\ & + \mathbf{G}_{P-v}\mathbf{Z}_{L\_\mathrm{GFM}}\mathbf{Tran}(\delta_0)) \end{aligned} \tag{50}$$

$$\begin{aligned}\mathbf{Z}_{\mathrm{GFM}}^{\mathrm{DFM}} = {} & \mathbf{Z}_L + \mathbf{V}_{\omega l}\mathbf{T}_{\omega\mathrm{GFM}} \\ & + \mathbf{Tran}(\delta_0)^{-1}(\mathbf{Z}_f + (\mathbf{V}_{\omega f} + \mathbf{G}_{f-\mathrm{DEL}})\mathbf{T}_{\omega\mathrm{GFM}}) \end{aligned} \tag{51}$$

where $\mathbf{G}_{P-i}$ is $[V_{d0}, 0]$ and $\mathbf{G}_{P-v}$ is $[I_{d0}, I_{q0}]$. G_{Droop} represents the transfer function of the droop controller as follows:

$$G_{\mathrm{Droop}} = \frac{G_p\omega_0}{s+\omega_0} \tag{52}$$

where G_p denotes the droop parameter. The matrix $\mathbf{Tran}(\delta_0)$ is introduced by the steady-state phase angle difference δ_0 between the terminals of the power cable as follows:

$$\mathbf{Tran}(\delta_0) = \begin{bmatrix} \cos(\delta_0) & \sin(\delta_0) \\ -\sin(\delta_0) & \cos(\delta_0) \end{bmatrix}. \tag{53}$$

$\mathbf{Z}_{L\_\mathrm{GFM}}$ represents the filter inductor of the GFM-VSC as

$$\mathbf{Z}_{L\_\mathrm{GFM}} = \begin{bmatrix} R_{\mathrm{GFM}} + sL_{\mathrm{GFM}} & -\omega_0 L_{\mathrm{GFM}} \\ \omega_0 L_{\mathrm{GFM}} & R_{\mathrm{GFM}} + sL_{\mathrm{GFM}} \end{bmatrix}. \tag{54}$$

$\mathbf{Z}_{\mathrm{Line}}$ represents the impedance of the power cable, which can be expressed as

$$\mathbf{Z}_{\mathrm{Line}} = \begin{bmatrix} R_{\mathrm{Line}} + sL_{\mathrm{Line}} & -\omega_0 L_{\mathrm{Line}} \\ \omega_0 L_{\mathrm{Line}} & R_{\mathrm{Line}} + sL_{\mathrm{Line}} \end{bmatrix}. \tag{55}$$

$\mathbf{V}_{\omega l}$ represents the voltage deviation on the power cable due to the fundamental frequency dynamics. Based on the analysis in Section III-D, $\mathbf{V}_{\omega l}$ can be expressed as

$$\mathbf{V}_{\omega l} = \left[-I_{q0}L_{\mathrm{Line}}, I_{d0}L_{\mathrm{Line}}\right]^T. \tag{56}$$

$\mathbf{V}_{\omega f}$ represents the voltage deviation on the filter inductor due to the fundamental frequency dynamics, which can be similarly derived by appropriately substituting the steady-state current and inductance values into (56). $\mathbf{G}_{f\text{-DEL}}$ represents the voltage deviation of the control delay due to the fundamental frequency dynamics, as previously derived in (37).

The solidness of (33) can then be proved by block diagram algebra similar to the analysis in Section IV-B, which is not included here due to the limited space. Simulation and experimental results will be provided in the following sections to validate the modeling equivalence. As a conclusion, the DFM and FFM of the studied interconnected system are equivalent to the block diagram in Fig. 8, proving the equivalence of system modeling in different reference frames. It also indicates that when $\mathbf{T}_{\omega\mathrm{GFM}}$ is known, $\mathbf{Z}_{\mathrm{GFM}}$ and $\mathbf{Z}_{\mathrm{GFM}}^{\mathrm{DFM}}$ can be transformed between each other by algebraic calculations.

D. Equivalence of System Stability Prediction in Different Reference System Frames

The stability of the studied system can be predicted based on the derived small-signal models in different reference frames. Assume that the controllers for both the GFL-VSC and GFM-VSC have been properly designed, which means that $\mathbf{Z}_{\mathrm{GFM}}$, $\mathbf{Y}_{\mathrm{GFL}}$, $\mathbf{T}_{\omega\mathrm{GFM}}$, $\mathbf{T}_{\omega\mathrm{GFL}}$, and $\mathbf{Z}_{\mathrm{GFM}}^{\mathrm{DFM}}$ have no right-half-plane (RHP) poles and system instability is mainly induced by the interaction between the GFM-VSC and GFL-VSC. Furthermore,

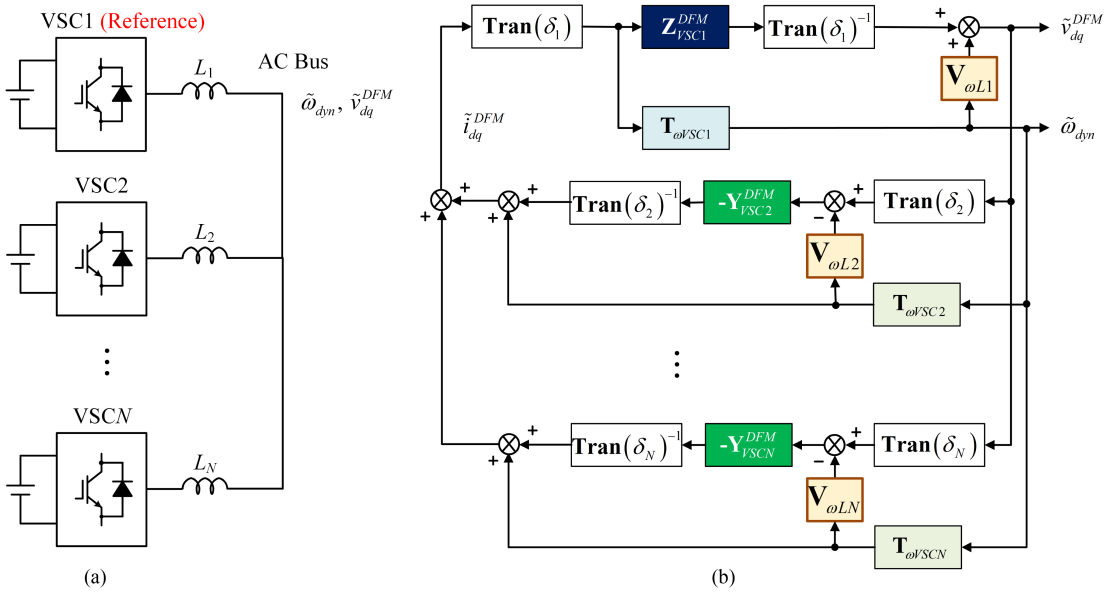

Fig. 12. (a) Diagram of a multiple-converter system. (b) Small-signal block diagram for the studied multiple-converter system.

from (33), it can be assumed that $\left(I-\frac{1}{s}\begin{bmatrix}I_{q0}\\-I_{d0}\end{bmatrix}\mathbf{T}_{\omega\mathrm{GFM}}\right)^{-1}$ has no RHP poles.

For DFM including fundamental frequency as terminal characteristics, the return ratio matrix $\mathbf{L}^{\mathrm{DFM}}$ can be derived as follows:

$$\mathbf{L}^{\mathrm{DFM}}=\mathbf{Y}_{\mathrm{GFL}}\mathbf{Z}_{\mathrm{GFM}}^{\mathrm{DFM}}-\mathbf{T}_{\omega\mathrm{GFL}}\mathbf{T}_{\omega\mathrm{GFM}}. \tag{57}$$

Substituting (32) and (33) into (57), it can be obtained that

$$\begin{aligned}\mathbf{L}^{\mathrm{DFM}}&=\mathbf{Y}_{\mathrm{GFL}}\mathbf{Z}_{\mathrm{GFM}}^{\mathrm{DFM}}-\left(\frac{1}{s}\left(-\mathbf{Y}_{\mathrm{GFL}}\right)\begin{bmatrix}0\\V_{d0}\end{bmatrix}+\frac{1}{s}\begin{bmatrix}I_{q0}\\-I_{d0}\end{bmatrix}\right)\mathbf{T}_{\omega\mathrm{GFM}}\\&=\mathbf{Y}_{\mathrm{GFL}}\left(\mathbf{Z}_{\mathrm{GFM}}^{\mathrm{DFM}}+\frac{1}{s}\begin{bmatrix}0\\V_{d0}\end{bmatrix}\mathbf{T}_{\omega\mathrm{GFM}}\right)-\frac{1}{s}\begin{bmatrix}I_{q0}\\-I_{d0}\end{bmatrix}\mathbf{T}_{\omega\mathrm{GFM}}\\&=\mathbf{L}-(\mathbf{I}+\mathbf{L})\frac{1}{s}\begin{bmatrix}I_{q0}\\-I_{d0}\end{bmatrix}\mathbf{T}_{\omega\mathrm{GFM}}\end{aligned} \tag{58}$$

where $\mathbf{L}$ denotes the return ratio matrix for FFM without fundamental frequency as terminal characteristics, which can be expressed as $\mathbf{L}=\mathbf{Y}_{\mathrm{GFL}}\mathbf{Z}_{\mathrm{GFM}}$. Based on the multivariable feedback control theory [37], system stability depends on whether there exist RHP poles for the determinant of $(\mathbf{I}+\mathbf{L}^{\mathrm{DFM}})^{-1}$ in DFM or the determinant of $(\mathbf{I}+\mathbf{L})^{-1}$ in FFM. Moreover, based on (58), we have

$$\left(\mathbf{I}+\mathbf{L}^{\mathrm{DFM}}\right)^{-1}=\left(\mathbf{I}-\frac{1}{s}\begin{bmatrix}I_{q0}\\-I_{d0}\end{bmatrix}\mathbf{T}_{\omega\mathrm{GFM}}\right)^{-1}(\mathbf{I}+\mathbf{L})^{-1}. \tag{59}$$

As $\left(\mathbf{I}-\frac{1}{s}\begin{bmatrix}I_{q0}\\-I_{d0}\end{bmatrix}\mathbf{T}_{\omega\mathrm{GFM}}\right)^{-1}$ is assumed to be free of RHP poles, it can be concluded that the determinants of $(\mathbf{I}+\mathbf{L}^{\mathrm{DFM}})^{-1}$ and $(\mathbf{I}+\mathbf{L})^{-1}$ will share identical RHP poles [37]. Therefore, the stability prediction results in different reference frames will also be identical.

In conclusion, the above analysis proves that the modeling accuracy and stability prediction for a general interconnected GFM-VSC and GFL-VSC system is effectively equivalent for both DFM and FFM, despite an additional frequency terminal when modeled in dynamic-frequency frame. The unification of both models can be achieved by incorporating frequency dynamics into terminal voltage/current signals.

E. Integration of Multiple Converters

The interconnected GFM-VSC and GFL-VSC system studied above can be regarded as a general representative of the multiple-converter system, as shown in Fig. 12(a). For such kind of system, the transformation between local and global *dq*-frame can be accomplished as follows.

1) In Fixed-Frequency Frame: As demonstrated in [15], each converter is initially modeled in its local system *dq*-frame and subsequently transformed into a global system *dq*-frame, typically established at the ac bus. Using VSC1 as an example, the transformation between the impedance model in the global and local *dq*-frames is achieved by

$$\mathbf{Z}_{\mathrm{VSC1}}^{\mathrm{global}}=\mathbf{Tran}(\delta_1)^{-1}\,\mathbf{Z}_{\mathrm{VSC1}}\mathbf{Tran}\,(\delta_1)\,. \tag{60}$$

The matrix $\mathbf{Tran}(\delta_1)$ represents the steady-state phase angle difference induced by the line inductance L_1, whose expression can be found in (53). $\mathbf{Z}_{\mathrm{VSC1}}^{\mathrm{global}}$ and $\mathbf{Z}_{\mathrm{VSC1}}$ represent the impedance in global and local *dq*-frames, respectively. System stability can then be evaluated by integrating the converter impedances in the global *dq*-frame.

2) In Dynamic-Frequency Frame: The integration of multiple-converter impedance models can still be performed at the ac bus, as demonstrated in [24] and [25]. First, one converter is selected as the reference to establish the dynamic-frequency system frame (typically a GFM-VSC). All other converters are then modeled with reference to this dynamic-frequency frame.

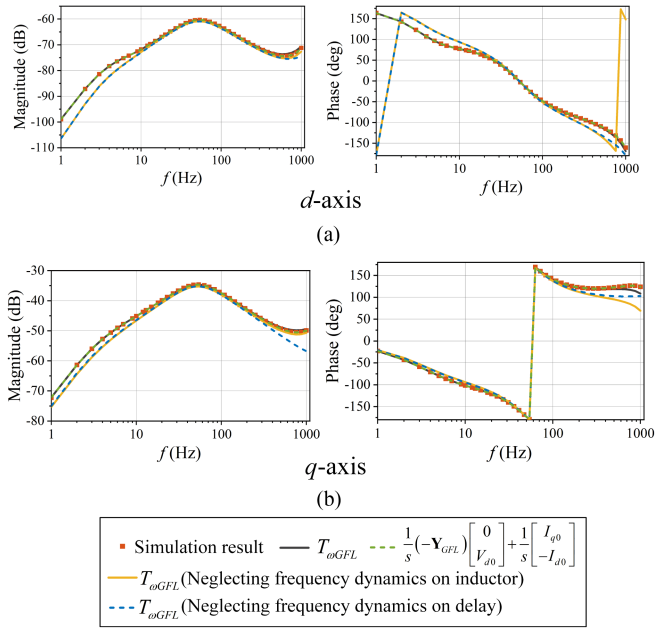

Fig. 13. Simulation and analytical results of $\mathbf{T}_{\omega\mathrm{GFL}}$. (a) On the d-axis. (b) On the q-axis.

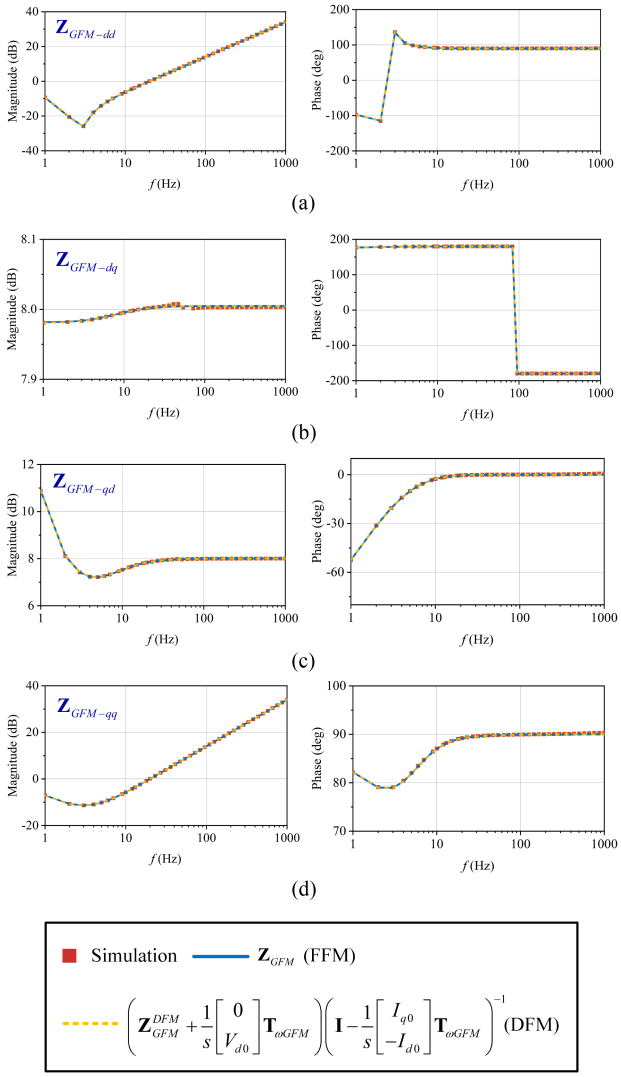

Fig. 14. Simulation and analytical results of $\mathbf{Z}_{\mathrm{GFM}}$, (a)–(d) represent the results of different channels.

The main difference is the formation of a frequency dynamic loop, which accounts for the additional frequency-related terminal in the impedance models. Furthermore, as pointed out in this article, frequency dynamics also takes effect on the modeling of inductors. Consequently, the overall small-signal block diagram for the studied multiple-converter system can be derived and presented in Fig. 12(b). For simplicity, only the impact of frequency dynamics on the inductor voltage $\mathbf{V}_{\omega Lx}$ is shown, while $\mathbf{Z}_{Lx}$ has already been incorporated into $\mathbf{Z}_{\mathrm{VSC1}}^{\mathrm{DFM}}$ or $-\mathbf{Y}_{\mathrm{VSC}x}^{\mathrm{DFM}}$ based on the basic circuit theory.

V. Simulation Validations

Simulations are conducted in this section to validate the effectiveness of the above analysis.

A. Model Equivalence Validations

Electromagnetic simulations in PSCAD/EMTDC are first conducted to validate the derived modeling equivalence.

1) For GFL-VSC: The relationship between $\mathbf{T}_{\omega\mathrm{GFL}}$ in DFM and $\mathbf{Y}_{\mathrm{GFL}}$ in FFM is validated. For the measurement of $\mathbf{T}_{\omega\mathrm{GFL}}$, a voltage source with varied frequency ω_{dyn} is used to emulate the fundamental frequency perturbations in the system [24], which can be expressed as follows:

$$\begin{aligned}\omega_{\mathrm{dyn}} &= \omega_0 + \tilde{\omega}_{\mathrm{dyn}}\\ \tilde{\omega}_{\mathrm{dyn}} &= A\sin(2\pi f t).\end{aligned} \tag{61}$$

A represents the amplitude of the frequency perturbation in the testing simulations, which is set as 0.2π rad/s (0.2% of the steady-state operating frequency ω_0). f represents the frequency of the injected perturbations, which will be scanned from 1 to 1000 Hz, covering the typical frequency range of fundamental frequency dynamics in the system. $\tilde{\boldsymbol{v}}_{dq}^{\mathrm{DFM}}$ is kept as zero by continuously aligning the system dq-frame to the integration of ω_{dyn}.

The dq-axis current response $\tilde{\boldsymbol{i}}_{dq}^{\mathrm{DFM}}$ is then measured and transfer function $\mathbf{T}_{\omega\mathrm{GFL}}$ is obtained, as shown in Fig. 13, together with the analytical results using the developed DFM and FFM. Comparison with models in the dynamic-frequency frame but neglecting frequency dynamics on the delay or filter inductance is also presented. It can be observed that the frequency dynamics on the control delay and filter inductance will influence the modeling accuracy, which is better to be considered when modeled in dynamic-frequency frame. The comparison of maximum absolute error between the modeling and simulation results is shown in Table III, supporting the effectiveness of the analysis in this paper.

2) For GFM-VSC: Simulation validation for GFM-VSC is then conducted. First, $\mathbf{Z}_{\mathrm{GFM}}$ is measured in the simulations by injecting external voltage perturbations of different frequencies into the GFM-VSC [36], which is compared with the impedance

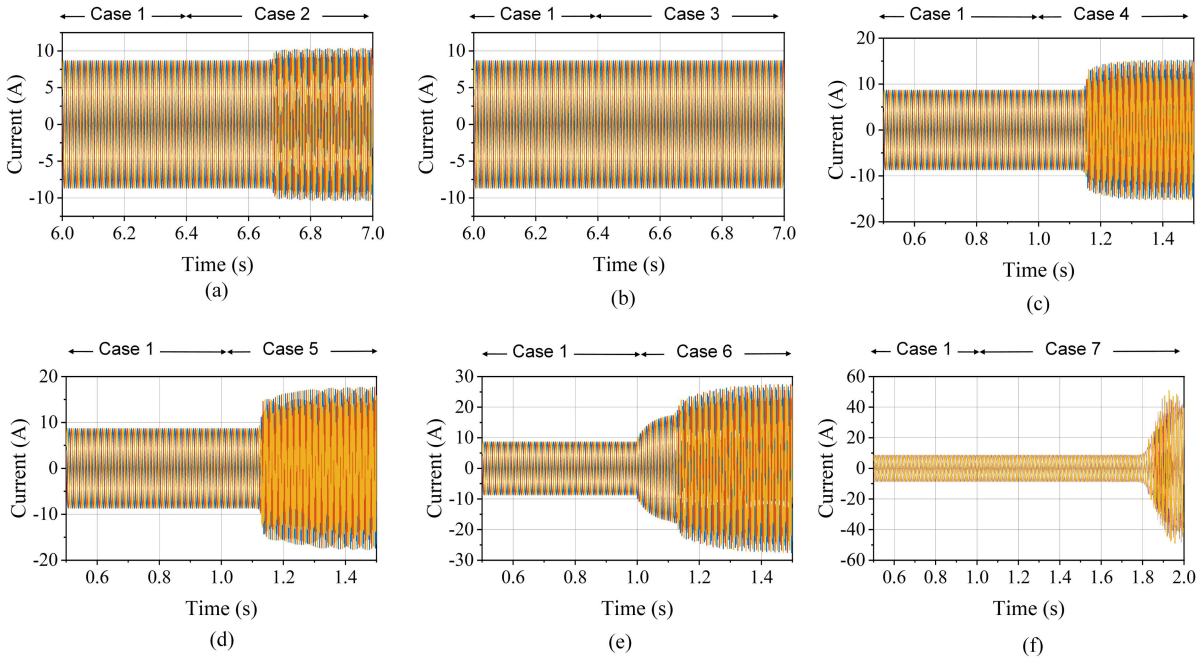

Fig. 15. Simulation results of different cases, (a)–(f) show the results from Case 1 to Case 7.

TABLE IV
VALIDATION CASES AND RHP POLES IN DIFFERENT FRAMES

Case No.	Parameter Adjustment	RHP Poles Calculated by DFM	RHP Poles Calculated by FFM
1	Original	—	—
2	$K_{pPLL} = 4.1$	(117.79, ±2610.58)	(117.79, ±2610.58)
3	$K_{pPLL} = 4.1$, $K_{pi} = 0.7$	—	—
4	$K_{pi} = 4.2$	(139.79, ±3860.30)	(139.79, ±3860.30)
5	$K_{ps} = 0.1$	(178.27, ±3360.94)	(178.27, ±3360.94)
6	$P_{ref} = 4$ kW	(93.57, ±2696.06)	(93.57, ±2696.06)
7	$G_p = 2.4$, $K_{pPLL} = 0.15$, $K_{iPLL} = 3.5$	(6.32, ±41.80)	(6.40, ±41.92)

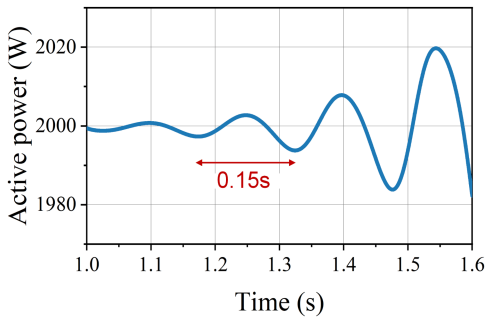

Fig. 16. Magnified view of active power variation in Case 7.

model in a fixed-frequency frame (FFM). The impedance calculated by (33) based on $\mathbf{Z}_{\mathrm{GFM}}^{\mathrm{DFM}}$ and $\mathbf{T}_{\omega\mathrm{GFM}}$ in DFM is also presented as a comparison. Simulation results are provided in Fig. 14.

It is shown that the measured converter impedance is consistent with the modeling results. More essentially, the solidness of (33) is proved, validating the correctness of model equivalence between DFM and FFM for GFM-VSC.

B. Stability Validations

Several representative cases have been selected for the validation of stability prediction results, as illustrated in Table IV, where different controller parameters (per-unit value) have been adjusted. Case 1 serves as the original case whose parameters are listed in Appendix A. The locations of RHP poles calculated by models in different reference frames have also been presented.

It is shown that the calculated RHP poles are identical in DFM and FFM with the same stability prediction results, validating the correctness of the theoretical analysis. For Case 7, a very large value of G_p has been assigned to consider very extreme cases with large frequency dynamics. Some singularity exists in the numerical calculation, causing a little deviation of the calculated RHP poles for different models, which will not influence the stability prediction in practice. It is shown that the interconnected GFM-VSC and GFL-VSC system tends to become unstable when increasing the proportional gain of the current controller, power controller, and PLL in the GFL-VSC as in Case 1–Case 5. Variation of the operation point may also lead to instability, which can be observed in Case 6. It is also shown in the analytical results that a large G_p may lead to the interaction of the GFM-VSC and GFL-VSCs at low frequencies, causing system resonance.

The time-domain simulation results validate the effectiveness of the stability prediction, with the waveforms of three-phase PCC current, as presented in Fig. 15. Furthermore, resonance frequency of Case 7 has also been identified to be 6.7 Hz in Fig. 16, which is consistent with the analytical results in Table IV, proving the accuracy of the small-signal modeling.

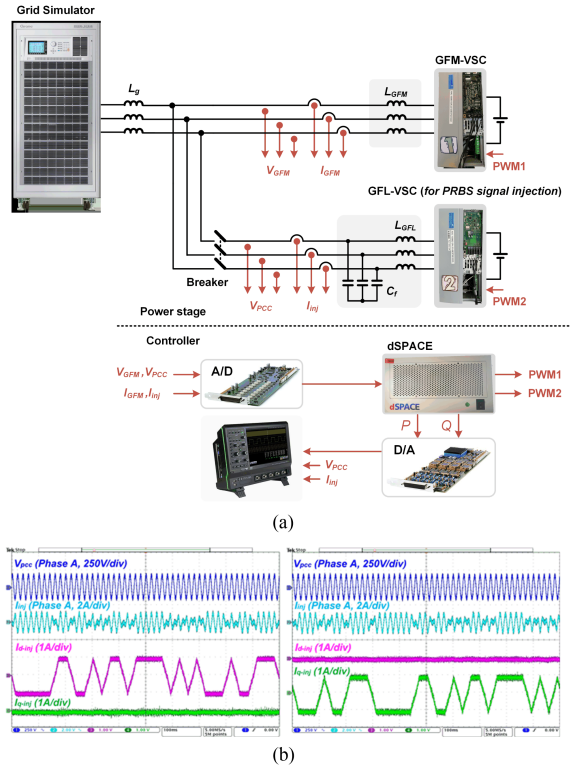

Fig. 17. (a) Experimental setup. (b) Injected PRBS perturbations in the dq-axis current I_{inj}.

VI. Experimental Validations

Experiments are further conducted for the validation.

A. Model Equivalence Validations

Considering the low magnitude of $\mathbf{T}_{\omega\mathrm{GFL}}$ (less than -60 dB for the d-axis and -30 dB for the q-axis), the validation for modeling equivalence of GFM-VSC is mainly conducted in this article. The experimental setup is shown in Fig. 17. Two Danfoss converters are controlled to act as GFL-VSC and GFM-VSC by dSPACE-1007. The control diagram for the GFM-VSC is the same, as presented in Fig. 4, and the GFL-VSC is used to generate perturbation signals for the impedance measurement. The current and voltage are measured by sensors and processed by the DS2004 A/D board. A DS2101 D/A board is used to transfer the measurements to the oscilloscope. The impedance measurement method in [36] is used, with pseudorandom binary sequence (PRBS) current perturbations in the dq-axis, as shown in Fig. 17(b), injected into the GFM-VSC for the measurements. The line inductance L_g is set as 7 mH. The frequency range of the measurement is set as 1–1000 Hz. Grid simulator Chroma 61845 is used.

The obtained impedance measurement result is shown in Fig. 18, together with the analytical impedance model $\mathbf{Z}_{\mathrm{GFM}}$ in FFM and the impedance model calculated by (33) using $\mathbf{Z}_{\mathrm{GFM}}^{\mathrm{DFM}}$ and $\mathbf{T}_{\omega\mathrm{GFM}}$ in DFM.

In the experimental case, G_p is increased to 0.032 p.u., with all the other parameters unchanged. This adjustment raises the low-frequency magnitude to reduce the measurement errors without impacting the effectiveness of the validation. It is shown that the measured converter impedance is consistent with the modeling results, validating the correctness of the model equivalence. Some deviations exist in the experiments due to the nonlinearity of inductors, errors from the measurement sensors, and dc-link dynamics.

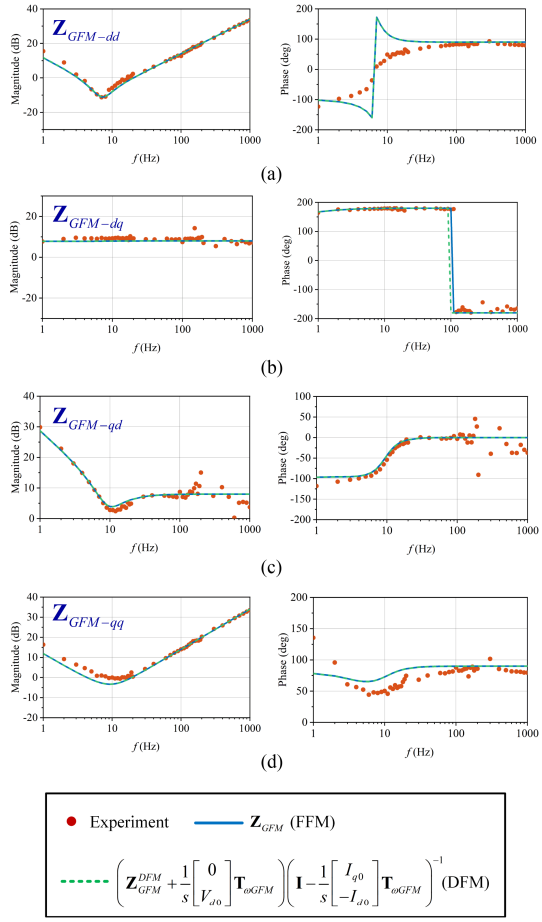

Fig. 18. Experimental and analytical results of $\mathrm{Z}_{\mathrm{GFM}}$, (a)–(d) represent the results of different channels.

B. Stability Validations

Stability prediction results are further validated, with the experimental setup, as shown in Fig. 19. The control diagram of the GFL-VSC is set according to Fig. 3.

The parameters of the power stage and the controller are included in Appendix A. The selected validation cases in Table IV are still used in the experiments.

Experimental results of different cases are shown in Fig. 20, where the active power, reactive power, voltage, and current (only showing Phase A) at PCC point have been recorded. It is shown that the system stability is consistent with the analytical and simulation results, validating the effectiveness of the above analysis. Furthermore, a magnified view of the collected waveforms in Case 7 has been presented in Fig. 21. A low-frequency resonance of 6.7 Hz can be observed, which is consistent with the theoretical analysis, proving the effectiveness of the modeling and stability analysis.

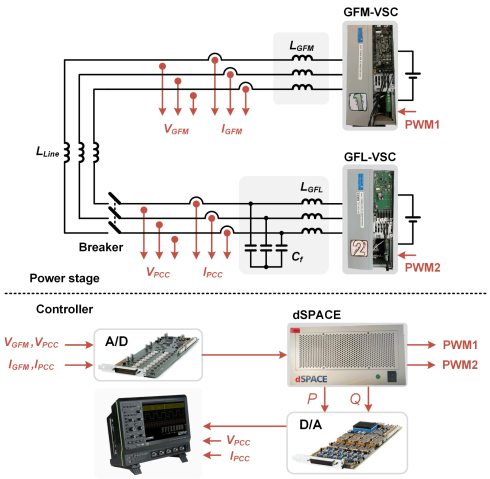

Fig. 19. Experimental setup for stability validations.

The proposed model equivalence also introduces practical advancements as follows.

1) Improved Modeling Accuracy of VSCs in the Dynamic-Frequency Frame: This article identifies the need to incorporate an additional term in the modeling of power stage and control delay to enhance the accuracy of converter modeling in the dynamic-frequency frame. For instance, Fig. 13 compares $\mathbf{T}_{\omega\mathrm{GFL}}$ for a GFL-VSC using the proposed model versus the conventional models that neglect the frequency dynamics on the power stage and control delay. It is shown that a deviation exists between the conventional models and the simulation results, outperformed by the proposed model.

2) Providing Flexibility for Reference-Frame Selection in Power-Electronic-Based Power Grid: Based on the improved impedance model in dynamic-frequency frame proposed in this article, the equivalence of impedance models in fixed-frequency and dynamic-frequency frames has been established at both the component and system levels. This finding offers greater flexibility in selecting reference frames for dynamic analysis of power-electronic-based power grid since the modeling in dynamic-frequency frame has been increasingly endorsed in recent research due to a larger integration of GFM-VSCs. This article reveals that the selection of reference system frame will not compromise the modeling accuracy: models in fixed-frequency frame provide more clarity, and models in dynamic-frequency frame effectively capture the interaction between synchronization controllers through the additional frequency-related terminal. Furthermore, the transformation and integration of models in different reference frames can also be conducted in a correct and flexible manner based on the proposed study, as presented in Section IV-E.

VII. Conclusion

This article has mathematically proved that the selection of reference frame will not influence the impedance modeling accuracy for VSC systems with fundamental frequency dynamics. First, model equivalence for the VSC components associated with system frame has been clarified. The modeling of control delay and power stage in dynamic-frequency frame has also proved to be effective in improving modeling accuracy. Furthermore, the system model in different frames is proved to be equivalent for an interconnected GFL-VSC and GFM-VSC system. The stability evaluation in different reference frames has also been unified. Finally, simulations and experiments have been conducted to validate the effectiveness of the theoretical analysis. It is proved that these two models in different reference frames are of equal accuracy and will both be applicable for future power-electronic-based power systems.

Appendix A
Parameters of the GFL-VSC and GFM-VSC

	Symbol	Description	Value
System	P_0	Rated power	2 kW (1 p.u.)
	V_g (f_0)	Voltage RMS	110 V (50 Hz) (1 p.u.)
GFL-VSC	L_{GFL}	Filter inductance	3 mH (0.07 p.u.)
	R_{GFL}	ESR of filter inductance	3 mΩ (2.4×10^{-4} p.u.)
	K_{pi}/K_{ii}	Inner current controller	2.8/70 (p.u.)
	K_{pPLL}/K_{iPLL}	PI controller of PLL (bandwidth = 100 Hz)	1.5/352.6 (p.u.)
	K_{ps}/K_{is}	Outer power controller	0.05/10 (p.u.)
	T_s	Sampling period	100 μs
GFM-VSC	L_{GFM}	Filter inductor	3 mH (0.07 p.u.)
	R_{GFM}	ESR of filter inductor	3 mΩ (2.4×10^{-4} p.u.)
	L_{Line}	Line inductor	5 mH (0.12 p.u.)
	R_{Line}	ESR of line inductor	5 mΩ (4.0×10^{-4} p.u.)
	G_p	Droop parameter	0.0032 (p.u.)
	ω_0	Cut-off frequency of the LPF in droop control	100π rad/s
	T_s	Sampling period	100 μs

Appendix B
Control Delay Model in Dynamic-Frequency Frame

Within the frequency range of interest, the expression of control delay on the three phases can be approximated based on (27) as follows:

$$\begin{cases} d_A^{\mathrm{del}} \approx d_A - T_d p d_A \\ d_B^{\mathrm{del}} \approx d_B - T_d p d_B \\ d_C^{\mathrm{del}} \approx d_C - T_d p d_C \end{cases} \tag{B.1}$$

where p denotes $\frac{d}{dt}$. Park's transformation as (B.2) is then applied to (B.1), which can be transformed to (B.3), with $\theta = \theta_0 + \tilde{\theta}_{\mathrm{dyn}}$ representing the dynamic-frequency frame

$$\mathbf{T}_{dq} = \sqrt{\frac{2}{3}} \begin{bmatrix} \cos\theta & \cos\left(\theta - \frac{2}{3}\pi\right) & \cos\left(\theta + \frac{2}{3}\pi\right) \\ -\sin\theta & -\sin\left(\theta - \frac{2}{3}\pi\right) & -\sin\left(\theta + \frac{2}{3}\pi\right) \\ \frac{\sqrt{2}}{2} & \frac{\sqrt{2}}{2} & \frac{\sqrt{2}}{2} \end{bmatrix} \tag{B.2}$$

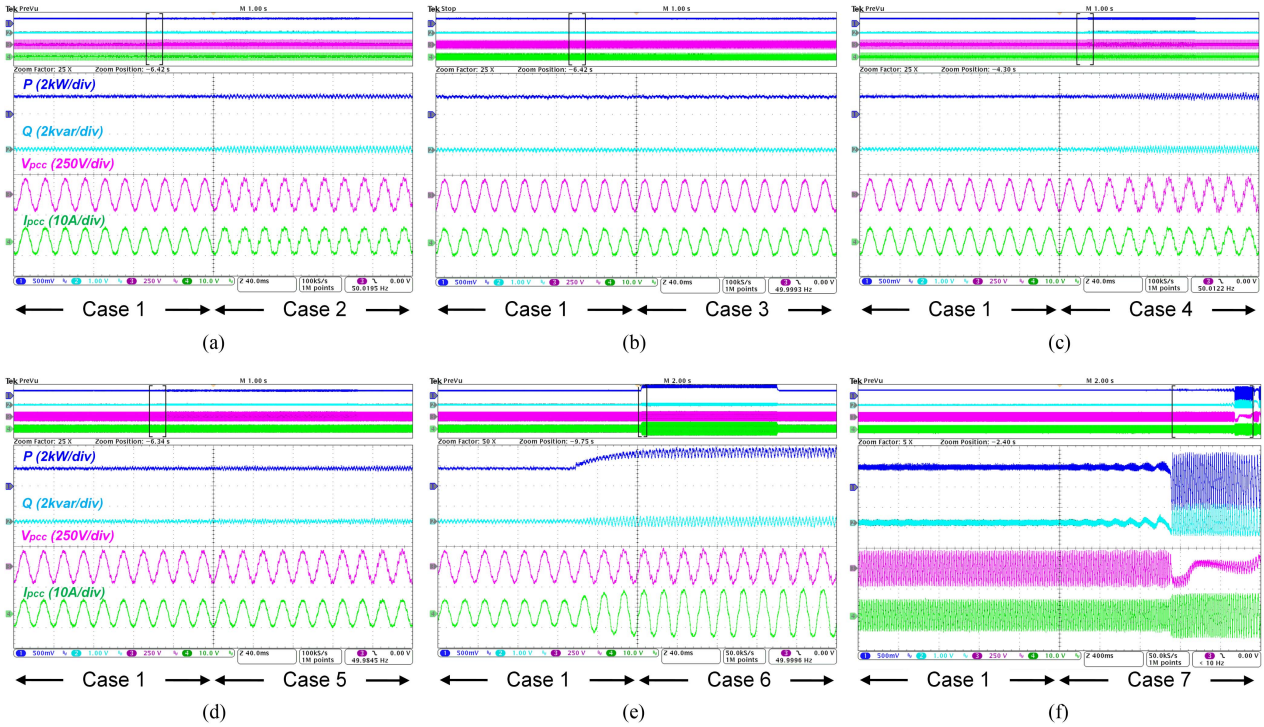

Fig. 20. Experimental results of different cases, (a)–(f) show the results from Case 1 to Case 7.

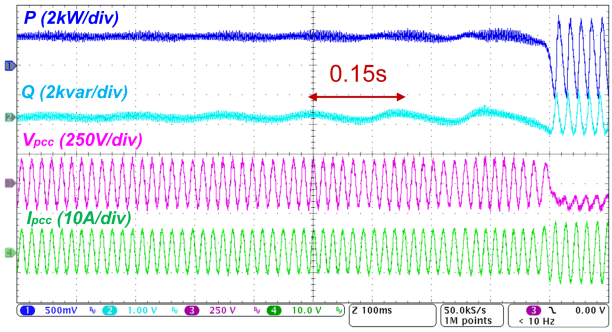

Fig. 21. Magnified view of waveforms in Case 7.

$$\mathbf{T}_{dq}\begin{bmatrix} d_A^{\text{del}} \\ d_B^{\text{del}} \\ d_C^{\text{del}} \end{bmatrix} \approx \mathbf{T}_{dq}\begin{bmatrix} d_A \\ d_B \\ d_C \end{bmatrix} - \mathbf{T}_{dq}T_d p\left(\mathbf{T}_{dq}^{-1}\begin{bmatrix} d_{d-\text{DFM}} \\ d_{q-\text{DFM}} \\ d_{o-\text{DFM}} \end{bmatrix}\right). \tag{B.3}$$

Hence, it can then be derived that

$$\begin{bmatrix} d_{d-\text{DFM}}^{\text{del}} \\ d_{q-\text{DFM}}^{\text{del}} \\ d_{o-\text{DFM}}^{\text{del}} \end{bmatrix} \approx \begin{bmatrix} d_{d-\text{DFM}} \\ d_{q-\text{DFM}} \\ d_{o-\text{DFM}} \end{bmatrix} - T_d\mathbf{T}_{dq}\mathbf{T}_{dq}^{-1}\begin{bmatrix} pd_{d-\text{DFM}} \\ pd_{q-\text{DFM}} \\ pd_{o-\text{DFM}} \end{bmatrix} - T_d\mathbf{T}_{dq}\left(p\mathbf{T}_{dq}^{-1}\right)\begin{bmatrix} d_{d-\text{DFM}} \\ d_{q-\text{DFM}} \\ d_{o-\text{DFM}} \end{bmatrix}. \tag{B.4}$$

The following equation can then be derived based on the expression of $\mathbf{T}_{dq}$ in (B.2):

$$-T_d\mathbf{T}_{dq}\left(p\mathbf{T}_{dq}^{-1}\right) = -T_d\begin{bmatrix} 0 & -(\omega_0+\tilde{\omega}_{\text{dyn}}) & 0 \\ \omega_0+\tilde{\omega}_{\text{dyn}} & 0 & 0 \\ 0 & 0 & 0 \end{bmatrix}. \tag{B.5}$$

Finally, (28) can be obtained by substituting (B.5) with (B.4).

Appendix C
Transfer Function Matrices for the GFL-VSC

Apart from the frequency-dynamics-related transfer function matrices in (34)–(38), the rest of the transfer function matrices in the block diagram can be expressed as follows:

$$\mathbf{G}_{PQ-i} = \begin{bmatrix} V_{d0} & 0 \\ 0 & -V_{d0} \end{bmatrix} \tag{C.1}$$

$$\mathbf{G}_{PQ-v} = \begin{bmatrix} I_{d0} & I_{q0} \\ -I_{q0} & I_{d0} \end{bmatrix} \tag{C.2}$$

$$\mathbf{G}_{PQ} = \begin{bmatrix} k_{ps}+\frac{k_{is}}{s} & 0 \\ 0 & -\left(k_{ps}+\frac{k_{is}}{s}\right) \end{bmatrix} \tag{C.3}$$

$$\mathbf{G}_{CI} = \begin{bmatrix} k_{pi}+\frac{k_{ii}}{s} & 0 \\ 0 & k_{pi}+\frac{k_{ii}}{s} \end{bmatrix} \tag{C.4}$$

$$\mathbf{G}_{\text{FF}} = \begin{bmatrix} 1 & 0 \\ 0 & 1 \end{bmatrix} \tag{C.5}$$

$$\mathbf{G}_{\text{DEL}} = \begin{bmatrix} \frac{1-0.5sT_d}{1+0.5sT_d} & 0 \\ 0 & \frac{1-0.5sT_d}{1+0.5sT_d} \end{bmatrix} \tag{C.6}$$

$$\mathbf{G}_{id} = \frac{V_{\text{dc}}}{(sL_{\text{GFL}} + R_{\text{GFL}})^2 + (\omega_0 L_{\text{GFL}})^2} \times \begin{bmatrix} sL_{\text{GFL}} + R_{\text{GFL}} & \omega_0 L_{\text{GFL}} \\ -\omega_0 L_{\text{GFL}} & sL_{\text{GFL}} + R_{\text{GFL}} \end{bmatrix} \quad \text{(C.7)}$$

$$\mathbf{Z}_f = \begin{bmatrix} sL_{\text{GFL}} + R_{\text{GFL}} & -\omega_0 L_{\text{GFL}} \\ \omega_0 L_{\text{GFL}} & sL_{\text{GFL}} + R_{\text{GFL}} \end{bmatrix}. \quad \text{(C.8)}$$

ACKNOWLEDGMENT

The authors would like to thank Prof. Paolo Mattavelli from the University of Padova and Prof. Dushan Boroyevich from Virginia Tech for their willingness to lend their expertise and insights to this work. Their invaluable feedbacks have undoubtedly improved the quality of this research.

REFERENCES

[1] X. Guo, X. Chen, Xia Chen, P. Sherman, J. Wen, and M. McElroy, "Grid integration feasibility and investment planning of offshore wind power under carbon-neutral transition in China," *Nature Commun.*, vol. 14, Apr. 2023, Art. no. 2447.

[2] Y. Li, Y. Gu, and T. C. Green, "Revisiting grid-forming and grid-following inverters: A duality theory," *IEEE Trans. Power Syst.*, vol. 37, no. 6, pp. 4541–4554, Nov. 2022.

[3] J. Fang, H. Deng, N. Tashakor, F. Blaabjerg, and S. M. Goetz, "State-space modeling and control of grid-tied power converters with capacitive/battery energy storage and grid-supportive services," *IEEE J. Emerg. Sel. Topics Power Electron.*, vol. 11, no. 1, pp. 234–250, Feb. 2023.

[4] D. Yang and X. Wang, "Unified modular state-space modeling of grid-connected voltage-source converters," *IEEE Trans. Power Electron.*, vol. 35, no. 9, pp. 9700–9715, Sep. 2020.

[5] R. Rosso, S. Engelken, and M. Liserre, "Robust stability investigation of the interactions among grid-forming and grid-following converters," *IEEE J. Emerg. Sel. Topics Power Electron.*, vol. 8, no. 2, pp. 991–1003, Jun. 2020.

[6] E. A. A. Coelho, P. C. Cortizo, and P. F. D. Garcia, "Small-signal stability for parallel-connected inverters in stand-alone AC supply systems," *IEEE Trans. Ind. Appl.*, vol. 38, no. 2, pp. 533–542, Mar./Apr. 2002.

[7] Y. Wang, X. Wang, F. Blaabjerg, and Z. Chen, "Harmonic instability assessment using state-space modeling and participation analysis in inverter-fed power systems," *IEEE Trans. Ind. Electron.*, vol. 64, no. 1, pp. 806–816, Jan. 2017.

[8] J. Lyu, X. Cai, and M. Molinas, "Frequency domain stability analysis of MMC-based HVDC for wind farm integration," *IEEE J. Emerg. Sel. Topics Power Electron.*, vol. 4, no. 1, pp. 141–151, Mar. 2016.

[9] R. W. Erickson and D. Maksimovic, *Fundamentals of Power Electronics*. New York, NY, USA: Springer, 2001.

[10] X. Wang, L. Harnefors, and F. Blaabjerg, "Unified impedance model of grid-connected voltage-source converter," *IEEE Trans. Power Electron.*, vol. 33, no. 2, pp. 1775–1787, Feb. 2018.

[11] A. Rygg, M. Molinas, C. Zhang, and X. Cai, "A modified sequence-domain impedance definition and its equivalence to the dq-domain impedance definition for the stability analysis of AC power electronic systems," *IEEE J. Emerg. Sel. Topics Power Electron.*, vol. 4, no. 4, pp. 1383–1396, Dec. 2016.

[12] J. Sun, "Small-signal methods for AC distributed power systems—A review," *IEEE Trans. Power Electron.*, vol. 24, no. 11, pp. 2545–2554, Nov. 2009.

[13] T. Xue, J. Lyu, Y. Li, H. Wang, and X. Cai, "A comprehensive study on impedance models of grid-tied voltage-source converters," in *Proc. 46th Annu. Conf. IEEE Ind. Electron. Soc.*, 2020, pp. 3118–3125.

[14] B. Wen, D. Boroyevich, R. Burgos, P. Mattavelli, and Z. Shen, "Analysis of D-Q small-signal impedance of grid-tied inverters," *IEEE Trans. Power Electron.*, vol. 31, no. 1, pp. 675–687, Jan. 2016.

[15] C. Zhang, M. Molinas, A. Rygg, and X. Cai, "Impedance-based analysis of interconnected power electronics systems: Impedance network modeling and comparative studies of stability criteria," *IEEE J. Emerg. Sel. Topics Power Electron.*, vol. 8, no. 3, pp. 2520–2533, Sep. 2020.

[16] R. Rosso, X. Wang, M. Liserre, X. Lu, and S. Engelken, "Grid-forming converters: Control approaches, grid-synchronization, and future trends—A review," *IEEE Open J. Ind. Appl.*, vol. 2, pp. 93–109, Apr. 2021.

[17] A. Sajadi, R. W. Kenyon, and B. Hodge, "Synchronization in electric power networks with inherent heterogeneity up to 100% inverter-based renewable generation," *Nature Commun.*, vol. 13, May 2022, Art. no. 2490.

[18] R. W. Kenyon, A. Sajadi, M. Bossart, A. Hoke, and B. Hodge, "Interactive power to frequency dynamics between grid-forming inverters and synchronous generators in power electronics-dominated power systems," *IEEE Syst. J.*, vol. 17, no. 3, pp. 3456–3467, Sep. 2023.

[19] A. Tayyebi, D. Groß, A. Anta, F. Kupzog, and F. Dörfler, "Frequency stability of synchronous machines and grid-forming power converters," *IEEE J. Emerg. Sel. Topics Power Electron.*, vol. 8, no. 2, pp. 1004–1018, Jun. 2020.

[20] Z. Zou et al., "Modeling and control of a two-bus system with grid-forming and grid-following converters," *IEEE J. Emerg. Sel. Topics Power Electron.*, vol. 10, no. 6, pp. 7133–7149, Dec. 2022.

[21] B. Wen, R. Burgos, D. Boroyevich, P. Mattavelli, and Z. Shen, "AC stability analysis and dq frame impedance specifications in power-electronics-based distributed power systems," *IEEE J. Emerg. Sel. Topics Power Electron.*, vol. 5, no. 4, pp. 1455–1465, Dec. 2017.

[22] D. P. Morán-Río, J. Roldán-Pérez, M. Prodanović, and A. García-Cerrada, "Influence of the phase-locked loop on the design of microgrids formed by diesel generators and grid-forming converters," *IEEE Trans. Power Electron.*, vol. 37, no. 5, pp. 5122–5136, May 2022.

[23] N. Bottrell, M. Prodanovic, and T. C. Green, "Dynamic stability of a microgrid with an active load," *IEEE Trans. Power Electron.*, vol. 28, no. 11, pp. 5107–5119, Nov. 2013.

[24] S. Wang, Z. Liu, J. Liu, D. Boroyevich, and R. Burgos, "Small-signal modeling and stability prediction of parallel droop-controlled inverters based on terminal characteristics of individual inverters," *IEEE Trans. Power Electron.*, vol. 35, no. 1, pp. 1045–1063, Jan. 2020.

[25] J. Yu, S. Wang, Z. Liu, J. Li, J. Liu, and J. Shang, "Accurate small-signal terminal characteristic model and SISO stability analysis approach for parallel grid-forming inverters in islanded microgrids," *IEEE Trans. Power Electron.*, vol. 38, no. 5, pp. 6597–6612, May 2023.

[26] Z. Liu, J. Liu, and D. Boroyevich, "Small-signal terminal characteristics modeling of three-phase boost rectifier with variable fundamental frequency," in *Proc. IEEE Appl. Power Electron. Conf. Expo.*, 2016, pp. 739–745.

[27] Z. Liu, J. Liu, D. Boroyevich, R. Burgos, and T. Liu, "Small-signal terminal characteristics modeling of three-phase droop-controlled inverters," in *Proc. IEEE Energy Convers. Congr. Expo.*, 2016, pp. 1–7.

[28] W. Cao, Y. Ma, F. Wang, L. M. Tolbert, and Y. Xue, "Low-frequency stability analysis of inverter-based islanded multiple-bus AC microgrids based on terminal characteristics," *IEEE Trans. Smart Grid*, vol. 11, no. 5, pp. 3662–3676, Sep. 2020.

[29] Y. Wu, H. Wu, F. Zhao, Z. Li, and X. Wang, "Influence of PLL on stability of interconnected grid-forming and grid-following converters," *IEEE Trans. Power Electron.*, vol. 39, no. 10, pp. 11980–11985, Oct. 2024.

[30] F. Cavazzana, A. Khodamoradi, H. Abedini, and P. Mattavelli, "Analysis of an impedance modeling approach for droop-controlled inverters in system DQ frame," in *Proc. IEEE Energy Convers. Congr. Expo.*, 2019, pp. 5576–5583.

[31] L. Harnefors, M. Bongiorno, and S. Lundberg, "Input-admittance calculation and shaping for controlled voltage-source converters," *IEEE Trans. Ind. Electron.*, vol. 54, no. 6, pp. 3323–3334, Dec. 2007.

[32] Y. Gu, Y. Li, Y. Zhu, and T. C. Green, "Impedance-based whole-system modeling for a composite grid via embedding of frame dynamics," *IEEE Trans. Power Syst.*, vol. 36, no. 1, pp. 336–345, Jan. 2021.

[33] "Deliverable 2.4: Requirement recommendations to adapt and extend existing grid codes," 2019. [Online]. Available: https://www.promotion-offshore.net/results/deliverables/

[34] L. Harnefors, M. Hinkkanen, U. Riaz, F. M. M. Rahman, and L. Zhang, "Robust analytic design of power-synchronization control," *IEEE Trans. Ind. Electron.*, vol. 66, no. 8, pp. 5810–5819, Aug. 2019.

[35] B. Wen, D. Boroyevich, R. Burgos, P. Mattavelli, and Z. Shen, "Inverse Nyquist stability criterion for grid-tied inverters," *IEEE Trans. Power Electron.*, vol. 32, no. 2, pp. 1548–1556, Feb. 2017.

[36] H. Gong, X. Wang, and D. Yang, "DQ-frame impedance measurement of three-phase converters using time-domain MIMO parametric identification," *IEEE Trans. Power Electron.*, vol. 36, no. 2, pp. 2131–2142, Feb. 2021.

[37] S. Skogestad and I. Postlethwaite, *Multivariable Feedback Control: Analysis and Design*. New York, NY, USA: Wiley, 2007.

Yang Wu (Member, IEEE) received the B.Eng. and Ph.D. degrees in electrical engineering from the Department of Electrical Engineering, Tsinghua University, Beijing, China, in 2017 and 2022, respectively.

She is currently a Marie Skłodowska-Curie Postdoctoral Researcher with the Department of Energy, Aalborg University, Aalborg, Denmark. Her research interests include modeling and stability analysis of power electronic converters, and condition monitoring of electrical assets.

Dr. Wu was a recipient of EU Marie Skłodowska-Curie Postdoctoral Fellowship, IEEE IAS PhD Thesis Award, Outstanding PhD Graduate Award from Beijing Ministry of Education, Excellent Graduate Award from Tsinghua University, and Two Best Paper and Presentation Awards at International Conferences.

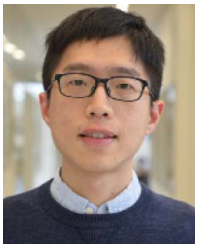

Heng Wu (Senior Member, IEEE) received the B.S. and M.S. degrees from the Nanjing University of Aeronautics and Astronautics, Nanjing, China, in 2012 and 2015, respectively, and the Ph.D. degree from Aalborg University, Aalborg, Denmark, in 2020, all in electrical engineering.

He is currently an Assistant Professor and a Leader of Electronic Power Grid Research Group with AAU Energy, Aalborg University. From 2015 to 2017, he was an Electrical Engineer with NR Electric Company Ltd., Nanjing. He was a Guest Researcher with Ørsted Wind Power, Fredericia, Denmark, in 2018, and Bundeswehr University Munich, Munich, Germany, in 2019. From 2020 to 2021, he was a Postdoctoral Researcher with Aalborg University. His research interests include the modeling and stability analysis of the power electronic based power systems.

Dr. Wu is the Chairman of the IEEE Task Force on Frequency-Domain Modeling and Dynamic Analysis of HVDC and FACTS, the subgroup leader of Cigre WG B4/C4.93 and Cigre WG B4.101, and the expert member of GB grid-forming best practice expert group formed by National Grid ESO, U.K. He was identified as the world's top 2% scientist by Stanford University in 2019. He was a recipient of the 2023 IEEE TRANSACTIONS ON POWER ELECTRONICS PRIZE PAPER AWARD, the 2019 Outstanding Reviewer Award of the IEEE TRANSACTIONS ON POWER ELECTRONICS, and the 2021 Star Reviewer Award of the IEEE JOURNAL OF EMERGING AND SELECTED TOPICS IN POWER ELECTRONICS.

Fangzhou Zhao (Member, IEEE) received the B.S. degree in electrical engineering and automation from the University of Electronic Science and Technology of China, Chengdu, China, in 2014, and the Ph.D. degree in electrical engineering from Xi'an Jiaotong University, Xi'an, China, in 2019.

He was a Postdoctoral Researcher with Aalborg University, Aalborg, Denmark, from 2020 to 2022. He is currently an Assistant Professor with AAU Energy, Aalborg University. His research interests include modeling and stability analysis of power electronics-based power systems, grid-forming control design, and grid emulation systems.

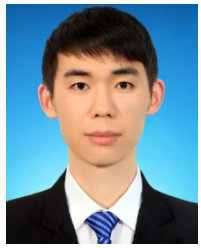

Zichao Zhou received the B.S. degree in electrical engineering and automation and the M.S. degree in electrical engineering from the Harbin Institute of Technology, Harbin, China, in 2017 and 2019, respectively. He is currently working toward the Ph.D. degree in power electronic engineering with the KTH Royal Institute of Technology, Stockholm, Sweden.

His research interests include the modeling and stability analysis of power electronics' systems.

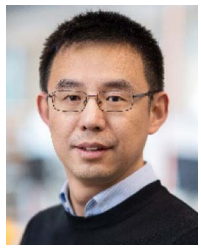

Xiongfei Wang (Fellow, IEEE) received the B.S. degree in electrical engineering from Yanshan University, Qinhuangdao, China, in 2006, the M.S. degree in electrical engineering from the Harbin Institute of Technology, Harbin, China, in 2008, and the Ph.D. degree in energy technology from Aalborg University, Aalborg, Denmark, in 2013.

From 2009 to 2022, he was with Aalborg University where he became an Assistant Professor in 2014, an Associate Professor in 2016, and has been a Professor and the founding Leader of Electronic Power Grid Research Group in 2018. Since 2022, he has been a Professor with the KTH Royal Institute of Technology, Stockholm, Sweden, and a Part-time Professor with Aalborg University. Since 2023, he has been a Visiting Professor with Hitachi Energy Research Center, Vasteras, Sweden. His research interests include modeling and control of power electronic converters, stability and power quality of power-electronic-dominated power systems, and high-power electronic systems.

Dr. Wang currently serves as an Editor-in-Chief for IEEE TRANSACTIONS ON POWER ELECTRONICS, the Chair of the IEEE International Roadmap on High-Power Electronics for Modern Energy Grids, and the Chair of IEEE Power Electronics Society (PELS) Technical Committee (TC 8) on Electronic Power Grid Systems. He was a recipient of 11 IEEE Prize Paper Awards, the 2016 AAU Talent for Future Research Leaders, the 2018 IEEE Richard M. Bass Outstanding Young Power Electronics Engineer Award, the 2019 IEEE PELS Sustainable Energy Systems Technical Achievement Award, and the 2022 Isao Takahashi Power Electronics Award.